Nano Research

Open Access

Research Article

Multicomponent nanoassembly integrating photosensitizer and Astragalus polysaccharide adjuvant for amplified photoimmunotherapy via hypoxia adaptation disruption

Chenjing Zhao[1,§], Yun Zhang[1,§], Xinrui Bao[1], Hexin Gong[1], Ze Wu[1], Wenwen Zang[1], Jinghong Hu[1], Tengfei Ji[2] ✉, and Zhengqi Dong[1] ✉

[1] *State Key Laboratory of Quality Ensurance and Sustainable Use of Dao-Di Herbs, Chinese Academy of Medical Sciences & Peking Union Medical College (CAMS), Institute of Medicinal Plant Development (IMPLAD), Beijing 100193, China*

[2] *State Key Laboratory of Bioactive Substance and Function of Natural Medicines, Institute of Materia Medica, Chinese Academy of Medical Sciences and Peking Union Medical College, Beijing 100050, China*

[§] *Chenjing Zhao and Yun Zhang contributed equally to this work.*

Cite this article: *Nano Research*, **2026**, *19*, 94908620. https://doi.org/10.26599/NR.2026.94908620

ABSTRACT: Photoimmunotherapy (PIT) employs photosensitizers that generate reactive oxygen species (ROS) under near-infrared laser irradiation to induce immunogenic cell death (ICD) and trigger systemic antitumor immunity. However, the hypoxic conditions within tumors markedly reduce photosensitization efficiency and therapeutic efficacy. Moreover, insufficient immune activation together with the profoundly suppressive tumor immune microenvironment further compromises treatment outcomes. Given these challenges, it is imperative to develop an integrated therapeutic platform capable of effectively overcoming these limitations. Here, a responsive delivery system has been developed that utilizes ROS and incorporates the immunomodulatory agent Astragalus polysaccharide (APS). Hydrophobic rapamycin (RAPA) is linked to the APS backbone through an ROS-sensitive thioether TK bond, forming the amphiphilic APS-TK-RAPA (ATKR) conjugate. Subsequently, the photosensitizer 2-(1-hexyloxyethyl)-2-devinyl pyropheophorbide-a (HPPH) is integrated into the system. The designed ATKR conjugate carrier facilitates the maturation of dendritic cells (DCs), effectively captures antigens released during PDT, and enhances antigen presentation. This further amplifies the adaptive immune response mediated by the APS-based carrier, thereby strengthening antitumor efficacy. In summary, ATKR with superior biocompatibility effectively surmounts the delivery challenges of hydrophobic photosensitizers. Moreover, it offers a promising nanoscale platform to address the critical issue of hypoxia in photodynamic therapy for cancer, serving as an effective inducer for augmenting immune responses.

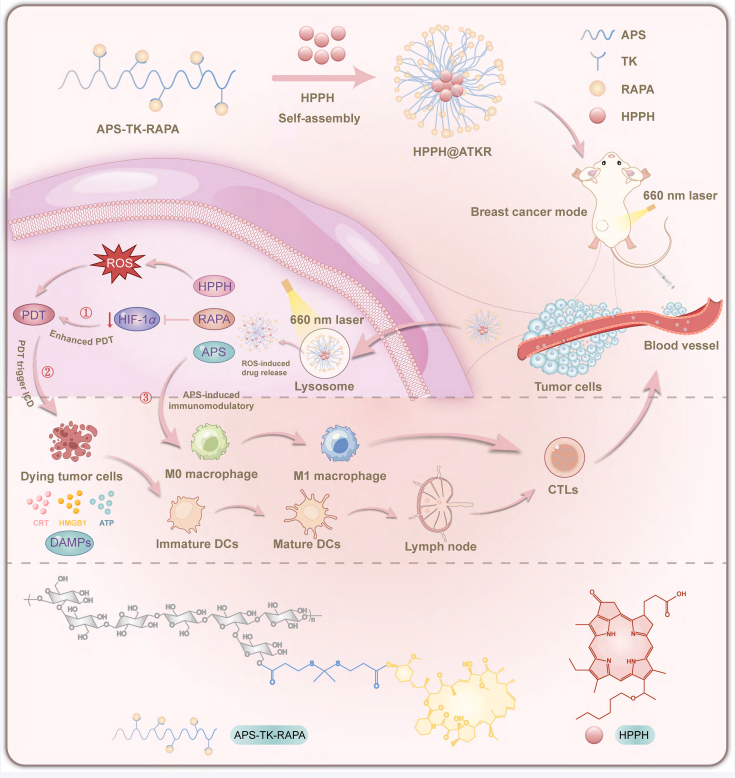

KEYWORDS: nanoassembly, photoimmunotherapy, immunogenic cell death, Astragalus polysaccharide adjuvant, tumor hypoxia resistance

Received: November 26, 2025; **Revised:** March 6, 2026; **Accepted:** March 6, 2026

✉Address correspondence to Tengfei Ji, jitf@imm.ac.cn; Zhengqi Dong, zqdong@implad.ac.cn

1 Introduction

The inherent complexity of cancer and its resistance to conventional therapeutic approaches render it one of the most challenging diseases to effectively treat to date. Even in the case of superficial tumors amenable to surgery, such as oral cancer, esophageal cancer, and cutaneous squamous cell carcinoma, mortality rates remain elevated due to factors including local invasion, high recurrence rates, and drug resistance [1–3]. Photodynamic therapy (PDT), a non-invasive treatment method, has been extensively employed in managing superficial tumors, particularly advantageous for patients who are ineligible for surgery, chemotherapy, or radiotherapy. Nonetheless, clinical data reveals that the five-year survival rates remain below 20% for advanced oral cancer, 13%–18% for esophageal cancer, and approximately 15% for melanoma, highlighting the significant challenges that persist in the clinical application of PDT [4–6]. 2-(1-Hexyloxyethyl)-2-vinylphthalocyanine-a (HPPH) is a highly efficient photosensitizer derived from chlorophyll-like compounds. In comparison to conventional photosensitizers, such as aluminum titanium phthalocyanine chloride, HPPH exhibits enhanced tissue penetration and excitation efficiency [7]. Through mechanisms involving excited-state electron transfer and intersystem crossing (ISC), HPPH produces reactive oxygen species (ROS), including singlet oxygen ($^1O_2$) and hydroxyl radicals (·OH). These ROS induce damage to tumor cell membranes, mitochondria, and DNA, ultimately resulting in tumor cell apoptosis.

Despite these advantageous properties, HPPH continues to encounter several critical challenges in clinical application [8]. Firstly, the preparation of HPPH involves its dissolution in ethanol and Tween 80, followed by suspension in a glucose solution, which constrains both its effective delivery and safety profile [9, 10]. To improve the delivery efficiency, various nanocarriers such as polymeric micelles and albumin complexes have been explored to enhance HPPH solubility and tumor accumulation. However, most conventional platforms function as passive reservoirs with sluggish release kinetics, failing to trigger a potent cascaded activation for efficient intracellular cargo liberation [11, 12]. Secondly, the hypoxic microenvironment characteristic of tumor cells, along with their inherent tolerance to hypoxia, suppresses the activation efficacy of HPPH. Lastly, although HPPH induces tumor cell death and promotes the release of damage-associated molecular patterns (DAMPs), considered a critical initiating event for immunotherapy, its immune-activating effects often fail to fully amplify [13]. Tumor cells may further suppress immune responses through mechanisms of immune evasion, thereby leading to the emergence of drug resistance. Therefore, overcoming hypoxia-induced resistance, optimizing the delivery system, and effectively activating immune responses are pivotal strategies for improving HPPH's therapeutic efficacy.

The hypoxic microenvironment characteristic of tumor cells represents a major constraint on the effectiveness of photosensitizers [14]. Therefore, the identification of appropriate sensitizing agents, particularly through the investigation of potential candidates among existing approved pharmaceuticals, has become an important research direction. Rapamycin (RAPA), a potent systemic metabolic regulator, exerts its effects by inhibiting key metabolic and proliferative pathways via modulation of the mTOR signaling cascade [15, 16]. Although RAPA has received FDA approval for the treatment of certain malignancies, its efficacy as a monotherapy remains suboptimal, primarily due to the mTORC2 negative feedback loop [17, 18]. Notably, when combined with PDT, RAPA demonstrates a pronounced synergistic enhancement of antitumor efficacy. RAPA enhances sensitivity of tumor cells to PDT-induced oxidative stress by disrupting the nuclear translocation of the nuclear factor erythroid 2-related factor 2 (NRF2) protein and inhibiting the activation of downstream antioxidant genes such as NQO1 and HO-1, while also regulating mTORC1 to suppress glycolytic pathways in tumor cells, thereby weakening their antioxidant defense systems [19]. Furthermore, RAPA modulates autophagy through the inhibition of Akt phosphorylation, transforming autophagy from a protective process into one that promotes cell death [20]. Concurrently, RAPA and PDT exhibit synergistic effects in the suppression of tumor angiogenesis: while PDT induces acute damage to tumor microvasculature, RAPA persistently inhibits vascular regeneration by downregulating hypoxia-inducible factor-1 alpha (HIF-1α) expression. Building upon this rationale, prior researches have explored the co-delivery of mTOR inhibitors with photosensitizers for tumor therapy. For example, the combination of RAPA with PDT has been employed in managing cutaneous photocarcinogenesis [19]. Additionally, RAPA paired with methyl 5-aminolevulinate has been used for human cutaneous squamous cell carcinoma (cSCC) [21]. Furthermore, nanodelivery platforms have been developed to facilitate the simultaneous delivery of verteporfin and Torin1 for tumor therapy.

The effectiveness of photosensitizers is influenced not only by the hypoxic conditions within the tumor microenvironment but also by the modulation of immune responses. Although PDT induces tumor cell damage and promotes the release of DAMPs (e.g., high mobility group box 1 (HMGB1), adenosine triphosphate (ATP), and heat shock proteins (HSPs)), the tumor microenvironment still impedes the immune system's ability to recognize tumor antigens leading to tumor recurrence [22]. A critical factor is the suboptimal capacity of dendritic cells (DCs) to present tumor antigens effectively. Inspired by the "Qi-tonifying" (immunostimulatory) bioactivity of traditional medicine [23, 24]. Our previous researches have demonstrated that a low-molecular-weight, highly branched polysaccharide fraction (branched at o-6 in α-1,4,6-glc*p*) derived from *Astragalus membranaceus* (APS) functions as a potent immune adjuvant [25, 26]. Distinct from common polysaccharides like chitosan or hyaluronic acid, APS possesses a definitive track record of clinical safety and triggers DC maturation via the Toll-like receptor 4 (TLR4) pathway [27–29]. Notably, beyond its immunomodulatory role, APS exhibits characteristics of a polymeric material capable of forming carriers with hydrophilic coatings [30]. This property facilitates the efficient delivery of therapeutic agents of RAPA and HPPH, ensuring their targeted release at the tumor site, thereby enhancing overall therapeutic efficacy.

In this study, we developed an ROS-responsive delivery system derived from APS. Using thioether ketone (TK) as an ROS-sensitive linker, the hydrophobic drug RAPA was covalently attached to the backbone of APS to form a novel APS-TK-RAPA (ATKR) conjugate, which could co-assemble with HPPH to obtain the nanomedicine formulation HPPH@ATKR. This delivery system integrates HPPH, RAPA, and APS, thereby facilitating the synergistic interaction of multiple antitumor therapeutic mechanisms. By optimizing the proportions of HPPH, RAPA, and APS, the designed self-assembled nanomedicine demonstrates uniform particle size, excellent drug-loading efficiency, and robust

long-term stability. Moreover, following intravenous injection, these self-assembled nanomedicines preferentially accumulate at tumor sites through the enhanced permeability and retention (EPR) effect. Specifically, the endogenous ROS in the tumor microenvironment initiates TK cleavage, while the subsequent light-triggered HPPH activation generates a singlet oxygen burst to accelerate carrier disintegration, thereby ensuring a highly targeted and robust intracellular cargo release via a positive feedback loop. Crucially, RAPA inhibits the mTOR signaling pathway to enhance cellular sensitivity to oxidative stress and downregulates HIF-1α, thereby alleviating hypoxia from its metabolic origin. Concurrently, APS activates DCs and enhances the immune response to bolster adaptive immunity (Fig. 1). In conclusion, this study proposes an innovative self-assembling drug delivery system which holds excellent clinical application prospects through the synergistic effect of HPPH, RAPA, and APS.

2 Experimental

2.1 Materials

Astragalus polysaccharides (APS) were purchased from Mackin (Shanghai, China). HPPH was purchased from MedChemExpress (New Jersey, USA). RAPA, and dimethyl aminopyridine (DMAP) were purchased from Aladdin (Shanghai, China). 1-(3-Dimethylaminopropyl)-3-ethylcarbodiimide hydrochloride (EDC·HCl) and N-hydroxy succinimide (NHS) were purchased from Shanghai yuanye Biotechnology Co., Ltd. (Shanghai, China). Dimethyl sulphoxide (DMSO) was purchased from Biotopped (Beijing, China). 9,10-Anthracenediyl-bis(methylene)dimalonic acid (ABDA), Hoechst 33342 (C1029), Reactive Oxygen Species Assay Kit (CA1410), the goat-anti-rabbit FITC conjugated secondary antibody (K1034G-AF488) and SAlexa Fluor @568 donkey anti-rabbit IgG (K1034D-AF568) were purchased from Solarbio Science & Technology Co.,

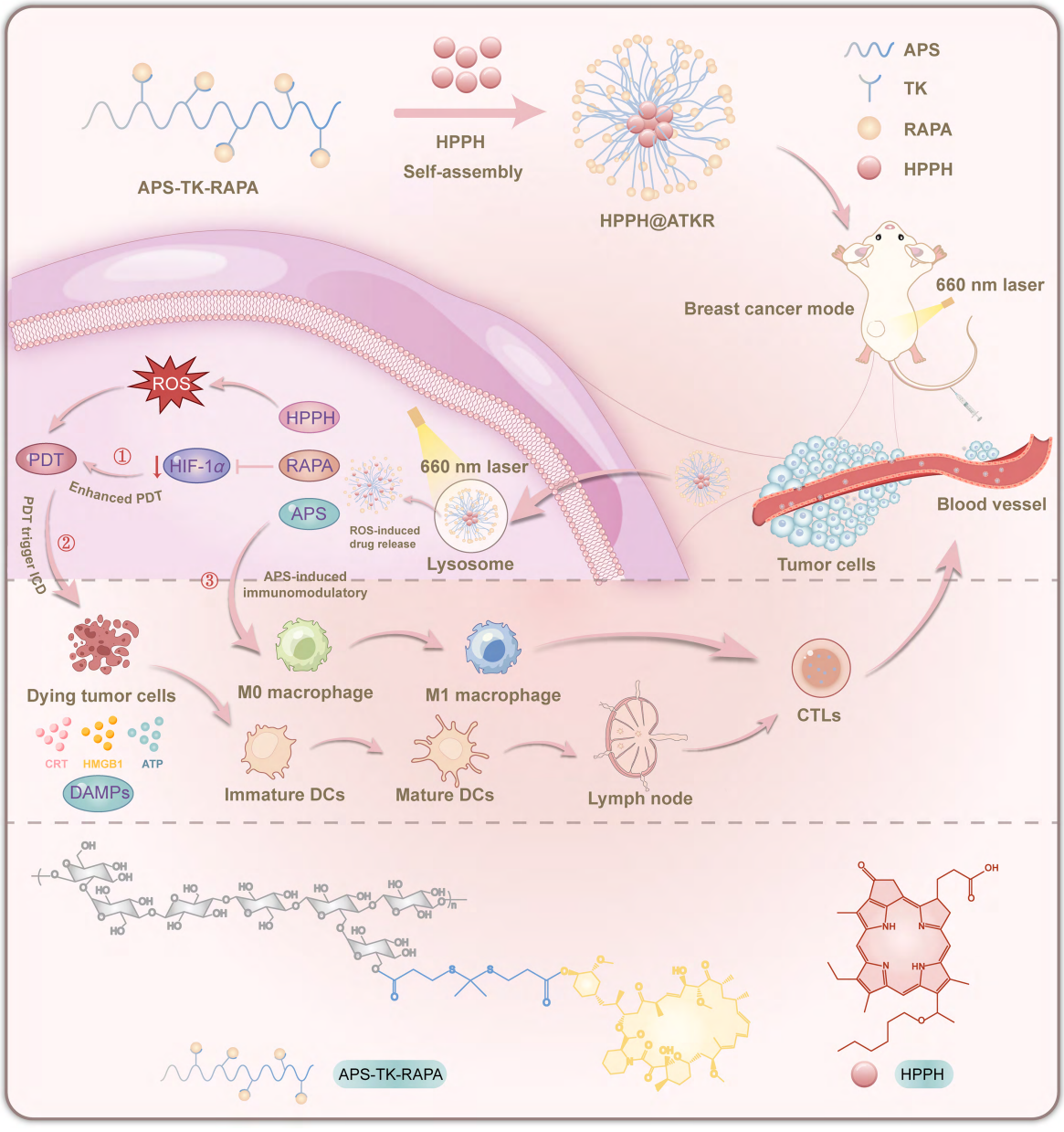

Figure 1 Schematic diagram illustrating HPPH@ATKR NP for breast cancer therapy under 660 nm laser.

Ltd. (Beijing, China). CCK-8 Kit (C0039), LysoTracker Green (C1047S), ATP Assay Kit (P0010), 4',6-diamidino-2-phenylindole (DAPI) (C1006), Annexin V-FITC Apoptosis Detection Kit (C1062S) were purchased from Beyotime Biotechnology (Shanghai, China).

The rabbit anti-calreticulin polyclonal antibody (27298-1-AP) and HMGB1 polyclonal antibody (10829-1-AP) were purchased from Proteintech Group, Inc. (Wuhan, China). Phycoerythrin (PE)-conjugated anti-mouse CD11c (117307), allophycocyanin (APC)-conjugated anti-mouse CD86 (105113), FITC-conjugated anti-mouse CD80 (104705) were purchased from Dakewe Biotech Co., Ltd. (Shenzhen, China). The PDT experiments were carried out by an XD-635AB Type Photodynamic Laser Therapy Instrument (660 nm, Guilin Xingda Optoelectronic Medical Device Co., Ltd., China).

2.2 Preparation of amphiphilic polysaccharides (APS-TK-RAPA)

2.2.1 Synthesis of TK linker

3-Mercaptopropionic acid (11.4 g, 108 mmol) and acetone (2.90 g, 49.1 mmol) were mixed in the presence of trifluoroacetic acid and stirred at room temperature for 6 h. A large number of crystals were produced, which were subsequently washed with *n*-hexane and cold water, and dried *in vacuo* to give a white solid as the resulting TK linker.

2.2.2 Synthesis of APS-TK-COOH

The –COOH group of thioketal-containing linker (TK) was activated by catalyst EDC·HCl and DMAP in DMSO using magnetic stirrer for 3 h at room temperature (R.T.). The molar ratio of TK:EDC·HCl:DMAP was 1:1.2:1.2. Subsequently, the activated TK/DMSO solution was added into the APS/DMSO solution drop by drop under continuous magnetic stirring at R.T. for additional 24 h. Afterwards, the obtained polymer was dialyzed against deionized water. The APS-TK-COOH was obtained by lyophilization.

2.2.3 Synthesis of APS-TK-RAPA

APS-TK-COOH (2 g), DMAP (0.23 g, 2 mmol), and EDC·HCl (0.77 g, 4 mmol) were dissolved in anhydrous DMSO (10 mL) and stirred at room temperature for 4 h to activate the carboxyl groups. The Rapamycin (RAPA, 0.91 g, 1 mmol) was added to the above mixture. After stirring at room temperature for 24 h, the obtained polymer was dialyzed with deionized water for 36 h. The supernatant was collected for freeze-drying, and APS-TK-RAPA was obtained.

2.3 Preparation and characterization of NPs

2.3.1 Preparation and characterization of polymeric nanoparticle

The polymeric nanoparticle was prepared through a combination of dialysis and solvent evaporation methods. Firstly, 5 mg of APS-TK-RAPA material was dissolved in 1 mL of DMSO and dialyzed in pure water using a dialysis bag (molecular mass cut off of 3500) for 24 h. During this period, the dialysis medium was changed three times, and at the end of the dialysis, the volume was fixed to 5 mL with pure water and then the ATKR micelle was obtained. In addition, 1 mg of HPPH was prepared by dissolving in 1 mL of anhydrous methanol, which was slowly added dropwise to the above solution under rapid stirring conditions (300 rpm/min) for 30 min. Afterwards, the methanol in the solvent was removed at 50 °C with a rotation speed of 160 rpm, followed by filtration through a 0.22 μm filter membrane to remove the unencapsulated free HPPH to obtain the HPPH@ATKR nanoparticles. The encapsulation efficiency (EE) was determined via ultrafiltration centrifugation (molecular weight cut off 10 kDa) and calculated as the weight ratio of encapsulated drug to the total drug added. The concentrations of RAPA and HPPH loaded in the nanoparticle were calculated by its standard curve (Fig. S1 in the Electronic Supplementary Material (ESM)) by high performance liquid chromatography (HPLC) and ultraviolet–visible spectroscopy (UV–Vis), respectively. The particle size, zeta potential, and morphology of the polymeric nanoparticles were determined by dynamic light scattering (DLS), transmission electron microscope (TEM) and scanning electron microscope (SEM).

2.3.2 Determination of critical micelle concentrations

We measured the critical micelle concentration (CMC) of ATKR NP using the pyrene probe method. First, pyrene was dissolved in methanol with the concentration of 12×10^{-6} mol/L as pyrene sample solution. 0.5 mL of the pyrene sample solution was accurately weighed into a 10-mL brown volumetric flask for total of 10 flasks. The solution in each flask was blow-dried under nitrogen gas. Then polymer solutions in gradient concentrations ranging from 0.01 to 100 μg/mL were added to each flask respectively. The volume in each flask was adjusted to the mark with deionized water, resulting in a final pyrene concentration of 6×10^{-7} mol/L. The flasks were sonicated for 30 min and then transferred to a 37 °C water bath where they were shaken for 12 h. 3 mL of each sample solution was taken and measured on a microplate reader (Thermo, USA). An excitation wavelength of 334 nm and an emission scan from 340 to 450 nm were used. The fluorescence intensity was measured at wavelengths of 372 nm (I_{372}) and 393 nm (I_{393}). The ratio I_{372}/I_{393} was cross-plotted against the logarithmic value of the sample concentration, log*C* (mg/mL) and CMC was calculated from this plot.

2.3.3 Light-activated drug release behavior

The light-activated drug release behavior of the polymeric nanoparticle was investigated using a modified dialysis method in the presence of 660 nm laser irradiation and/or H_2O_2. Briefly, 1 mL of HPPH@ATKR NP was sealed in dialysis bags (molecular mass cut off of 3500), and then incubated in 50 mL of phosphate buffer saline (PBS) containing 0, 1×10^{-3} M H_2O_2 or 2×10^{-2} M vitamin C with gentle shaking (100 rpm/min) at 37 °C. At predetermined time points, the laser group was placed under 660 nm laser irradiation at 200 mW/cm^2 for 5 min and then the medium for all groups was collected and replaced with prewarmed fresh PBS. The HPPH was quantified by UV–Vis.

2.3.4 ROS generation in vitro

In this part, we used ABDA as a probe to detect the ROS generation ability of the polymeric nanoparticle under 660 nm laser irradiation at 200 mW/cm^2. In details, 100 μL of 1 mg/mL ABDA solution was added to HPPH, HPPH@ATKR NP solutions (equivalent to 10 μg/mL of HPPH), which were deoxygenated and contained 1×10^{-4} M H_2O_2. Thereafter, the aforementioned solutions were exposed to 660 nm laser irradiation at 200 mW/cm^2. The ROS generation of the polymeric nanoparticle was evaluated by UV–Vis

spectroscopy at a preset time point.

2.4 Intracellular assay

2.4.1 *In vitro uptake efficiency*

The cellular uptake ability of the HPPH@ATKR NP was investigated using 4T1 cells. The cells were seeded into confocal dish with a density of 2×10^5. After incubation for 24 h, 2 mL of HPPH, HPPH@ATKR NPs (equivalent to 1 μg/mL of HPPH) was added, and the plates were incubated for another 1, 2, and 4 h. The cells were then washed with PBS three times, and the nuclei and lysosome of the cells were stained using Hoechst 33342 (10 μg/mL) and LysoTracker Green (66.67 nM) respectively prior to observation under CLSM.

The quantitative data of the cellular uptake efficiency were also investigated using flow cytometry. After the cells were co-incubated with NPs for different times, the cells were washed thrice with PBS, digested by trypsin and harvested by centrifugation at 1000 rpm for 5 min. Then the harvested cells were re-suspended in PBS. The fluorescence intensity of cells was measured by flow cytometer.

2.4.2 *In vitro induction of DC maturation*

4T1 cells were seeded in 6-well plates (2×10^5 cells per well) and cultured overnight. Then, RPMI 1640, HPPH, ATKR and HPPH@ATKR NPs were added and further cultured for 48 h. Afterwards, nanoparticle-treated tumor cell supernatant media were obtained after centrifugation at a speed of 12,000 rpm for 5 min. Dendritic cell line 2.4 (DC2.4) (2×10^5 cells per well in 6-well plates) were cultured with 50% obtained media plus 50% fresh media containing different formulations for 24 h.

Then, the DC2.4 cells were trypsinized, rinsed, and harvested. Before the surface antibody staining, the cells were incubated with Fc block for 15 min at room temperature. Last, anti-mouse CD11c-PE, anti-mouse CD80-FITC, and anti-mouse CD86-APC antibodies were used to stain the cells in a flow cytometry staining buffer for 30 min, and flow cytometry was used to examine the maturation of DC2.4 cells and data analysis was performed with FlowJo V10 Software. All quantitative results were obtained from at least three independent experiments.

2.4.3 *Intracellular ROS detection*

Inspired by the *in vitro* ROS generation ability, we further investigated the intracellular ROS generation ability via a 2',7'-dichlorofluorescin diacetate (DCFH-DA) probe. In short, the 4T1 cells were seeded into a 12-well plate with 1×10^5 cell/well in 1 mL of medium. After 24 h incubation, the HPPH, HPPH@ATKR NPs were added and incubated for 4 h, then the DCFH-DA (10 μM) was added into each well, after incubated for 20 min, used the fresh medium to replace the medium, and treated with 660 nm laser irradiation at 200 mW/cm^2 for 5 min (no laser group was used as Control). A fluorescence microscope and flow cytometry was used to detect the quality and quantity data of intracellular ROS level.

2.4.4 *In vitro cytotoxicity assay and cell apoptosis analysis*

The cytotoxicity of various nanoformulations was tested by Cell Counting Kit-8 (CCK-8) assay. The 4T1 cells were seeded into 96-well plates with 5×10^3 cells/well in 100 μL of medium. After overnight incubation, the medium was removed and replaced with 100 μL of medium containing PBS, HPPH, RAPA+HPPH, HPPH@ATKR NPs with different concentration for another 48 h of incubation. For the 660 nm laser group, after the above-mentioned drugs were added into the cells and cultured for 12 h, the groups were under 660 nm laser irradiation at 200 mW/cm^2 for 5 min and incubated for another 36 h, then followed by the standard CCK-8 assay method.

Moreover, we investigated the cell apoptosis of above-mentioned groups via the Annexin V-FITC apoptosis detection kit. Briefly, the 4T1 were seeded into a 6-well plate and incubated for 24 h, and added the above-mentioned groups and incubated for 12 h, then the laser groups were under 660 nm laser irradiation at 200 mW/cm^2 for 5 min and incubated for another 12 h before flow cytometry analysis.

2.4.5 *Western blotting analysis*

4T1 cells were treated with 500 μM $CoCl_2$ to induce hypoxia, except for the blank control group. Total protein was extracted using RIPA lysis buffer containing protease and phosphatase inhibitors and quantified by BCA assay. Equal amounts of protein (20 μg) were separated by SDS-PAGE and transferred onto PVDF membranes. The membranes were blocked with 5% non-fat milk for 1 h at R.T., then incubated overnight at 4 °C with primary antibodies against p-mTOR, mTOR, p-p70 S6K, p70 S6K and HIF-1α (all at 1:1000 dilution). After washing, membranes were incubated with HRP-conjugated secondary antibody (1:5000) for 1 h at R.T. Protein bands were visualized by ECL chemiluminescence, and the relative expression of target proteins was quantified by gray value analysis using ImageJ software with β-actin as the internal reference.

2.4.6 *Detection of crucial immunogenic cell death (ICD) biomarkers*

The surface-exposure of calreticulin (CRT) and extracellular released HMGB1 were assessed by immunofluorescence. For CRT exposure analysis, 4T1 cells were seeded and cultured in 12-well plate (1×10^5 cells/well) for 24 h. The cells were incubated with RPMI 1640, HPPH, HPPH@ATKR NPs (0.1 μg/mL based on HPPH) for 12 h. And then, cells were irradiated with or without 660 nm laser irradiation at 200 mW/cm^2 for 5 min as the light groups or non-light groups. Incubation was continued for 12 h and the medium was discarded. Next, the cells were fixed with 4% polyformaldehyde for 20 min at 37 °C and blocked with 5% bovine serum albumin (BSA) solution at R.T. for 1 h. After washing with PBS for 3 times, the cells were incubated with rabbit anti-calreticulin polyclonal antibody (1:500 dilution) at 4 °C overnight. Subsequently, the cells were further washed with PBS for 3 times and incubated with the goat-anti-rabbit FITC conjugated secondary antibody (1:1000 dilution) at R.T. for 1 h. After washing 3 times with PBS and staining with DAPI for another 10 min, the cells were then washed with PBS 3 times and observed by inverted fluorescence microscope with 405 and 488 nm lasers for visualizing nuclei and CRT expression on the cell membrane, respectively.

For HMGB1 release analysis, the procedure of cells treatments was performed as the assay of CRT exposure analysis. The differences were after cell fixation, permeabilization was performed with 0.5% Triton-X100 for 30 min and the primary and secondary antibodies were anti-HMGB1 antibody (1:200 dilution) and SAlexa Fluor@568 donkey anti-rabbit IgG (1:1000 dilution), respectively. And the lasers used to observe nuclei and HMGB1 expression were 405 and 568 nm, respectively.

The extracellular released ATP was determined using the ATP Assay Kit. 4T1 cells were seeded and cultured in 24-well plates (5×10^4 cells/well) for 24 h. The cells were treated with RPMI 1640,

HPPH, ATKR NPs (0.1 μg/mL based on HPPH) for 12 h. And then, cells were irradiated with or without 660 nm laser irradiation at 200 mW/cm^2 for 5 min as the light groups or non-light groups. The cell supernatant was collected after incubation for an additional 12 h. Finally, the release of ATP in the cell supernatant was measured by the ATP Assay Kit in accordance with the manufacturer's protocols.

2.4.7 *RNA sequencing measurement*

4T1 cells (1×10^6) were inoculated into 6-well plate overnight and incubated with RPMI-1640, HPPH@ATKR, HPPH@ATKR + Laser for 12 h. RNA-seq was conducted on Illumina NovaSeq platform (Majorbio, Beijing, China). Screening criteria followed fold change greater than 2 and P value less than 0.05, thereby differential expression genes (DEGs) were determined.

2.4.8 *Hemolysis assay*

The blood compatibility of the HPPH@ATKR NP was evaluated via the hemolysis assay at 10–100 μg/mL concentration before *in vivo* study. And the detailed procedures are appended in the supplementary data.

2.5 Animal experiments

2.5.1 *Animals*

BALB/c female mice (5–6 weeks old, ~ 20 g) were purchased from Beijing Vital River Laboratory Animal Technology Co., Ltd. All animal experiments were conducted in accordance with the National Institutes of Health Guide for the Care and Use of Laboratory Animals. All animal procedures were approved by the ethics committee of the Institute of Medicinal Plant Development (No. 20241205019). The orthotopic 4T1 tumor model was established by subcutaneous injection of 1×10^6 4T1 cells suspended in PBS (100 μL) at the second right mammary fat pad of the mice.

2.5.2 *In vivo antitumor study and immunofluorescence staining*

After the tumor volume reached around 100 mm^3, the tumor bearing mice were randomly divided into eight groups (n = 6): (1) Control group (PBS); (2) Control + Laser group, in which the mice were irradiated by a 660 nm laser at 200 mW/cm^2 for 5 min at the tumor sites; (3) HPPH + Laser group (2 mg/kg); (4) RAPA group (2 mg/kg); (5) HPPH + RAPA + Laser group; (6) ATKR group; (7) HPPH@ATKR group; (8) HPPH@ATKR + Laser group. The groups were treated with above-mentioned drugs through the tail vein intravenously three times, and the tumor volume and weight of mice were measured every other day. The tumor volume was calculated in accordance with the following formula: $0.5 \times L \times W^2$, where "L" represents the longest length of the tumor and "W" represents the shortest width across the center of the tumor. Finally, the mice were sacrificed and the tumor tissues and major organ tissues of all groups were collected for hematoxylin & eosin (H&E) staining. And the apoptosis, and hypoxia of tumor cells were investigated via TdT-mediated dUTP nick end labeling (TUNEL) staining, and immune-fluorescence staining methods.

To evaluate the ability of CRT exposure and HMGB1 release *in vivo*, the tumor slices were incubated with anti-calreticulin antibody or anti-HMGB1 antibody, then they were further incubated with goat-anti-rabbit FITC conjugated secondary antibody or donkey anti-rabbit IgG SAlexa Fluor @568 conjugated secondary antibody. After staining with DAPI, the obtained slices were observed by confocal laser scanning microscope (CLSM).

2.5.3 *Flow cytometry of immune response in vivo*

Tumors and draining lymph nodes (DLNs) were acquired from 4T1 tumor-bearing mice (n = 3–5 per group) experienced anti-tumor experiments. These tissues were ground and sieved to prepare single cell suspensions.

For the phenotypic analysis of activated dendritic cells (DCs), staining was performed using anti-mouse CD45-FITC, anti-mouse CD11c-PE, anti-mouse CD86-Bv-605, and anti-mouse CD80-PE-Cy7. To compare the cytotoxic effects on tumors following different drug treatments, tumor cells were stained with fluorescence conjugated anti-CD45, anti-CD3, anti-CD4 and anti-CD8 for the analysis of T cells. In the meantime, to examine alterations in macrophages, tumor cells were labeled with anti-CD45, anti-CD11b, anti-F4/80, anti-CD206, and anti-Gr-1. The stained immune cells were tested on flow cytometer (Berkman) and processed by FlowJo software.

2.6 Statistical analysis

All quantitative data are expressed as mean ± standard deviation (SD) ($n \geq 3$). Statistical significance was determined by one-way analysis of variance (ANOVA) followed by Tukey's post-hoc test using GraphPad Prism 10.0 software, with $P < 0.05$ considered statistically significant (*$P < 0.05$, **$P < 0.01$, ***$P < 0.001$, and ****$P < 0.0001$).

3 Results and discussion

3.1 Synthesis and characterization of the amphiphilic polysaccharide carrier (APS-TK-RAPA)

APS is a water-soluble polysaccharide [31]. To confer self-assembly and drug encapsulation capabilities, APS was chemically modified. Amphiphilic compound APS-TK-RAPA was synthesized by incorporating ROS-responsive TK linkages and subsequently conjugating the hydrophobic drug RAPA (Fig. 2(a)). The successful coupling reaction was confirmed through proton nuclear magnetic resonance spectroscopy (^{1}H NMR) and FTIR. Additionally, the loading capacity of RAPA within the synthesized amphiphilic material was quantified to be 24.74% using HPLC, with the standard curve of RAPA presented in Fig. S1(a) in the ESM.

In the ^{1}H NMR spectrum (Fig. 2(b)), the characteristic polysaccharide main chain peaks in APS were primarily localized in the δ 3.0–5.5 ppm range. For TK-COOH, a distinctive peak of $-CH_2-S-$ appeared at δ 2.5–3.0 ppm, and this signal was attributed to the methylene hydrogen in the thioacetal structure. The APS-TK-COOH retained the polysaccharide signal of APS and showed a new peak at δ 2.5–3.0 ppm, confirming the effective introduction of the TK structure. RAPA displayed characteristic signals both at δ 0.8–2.0 ppm (methyl/methylene groups of the aliphatic side chain) and δ 5.5–6.5 ppm (cycloalkene structure). In the ^{1}H NMR spectrum of APS-TK-RAPA, the characteristic peaks of APS, TK, and RAPA were observed simultaneously. This confirms the successful synthesis of the APS-TK-RAPA conjugate with a TK substitution degree of 1.02%. The high purity was further validated by the absence of residual small-molecule signals in Fig. 2(b) following exhaustive dialysis.

According to the infrared spectroscopic analysis (Fig. 2(c)), the

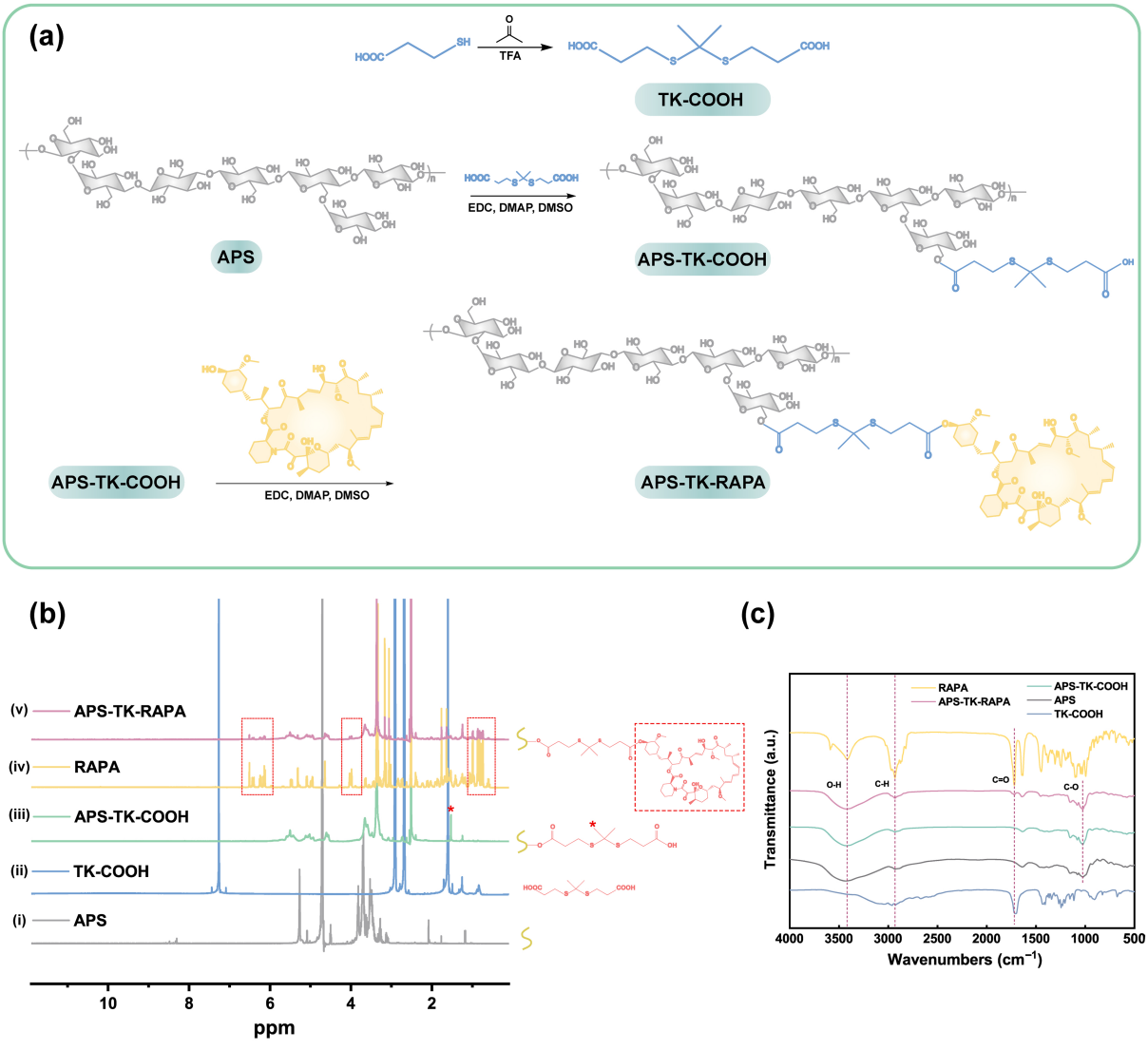

Figure 2 Synthesis and characterization of astragalus polysaccharide carrier. (a) Synthesis route of APS-TK-RAPA. (b) ^{1}H NMR spectra of (i) Astragalus polysaccharide (dissolved in D_2O), (ii) TK-COOH (dissolved in $CDCl_3$), (iii) APS-TK-COOH (dissolved in D_2O), (iv) RAPA (dissolved in DMSO-d_6), and (v) APS-TK-RAPA (dissolved in DMSO-d_6). (c) FTIR of APS, TK-COOH, APS-TK-COOH, RAPA, and APS-TK-RAPA.

broad absorption band observed at 3400 cm^{-1} in APS corresponded to the O–H stretching vibration, and triplet peaks in the range of 1000–1150 cm^{-1} were attributed to the C–O stretching vibrations of the polysaccharide backbone. In the APS-TK-COOH spectrum, a distinct peak at 1688.30 cm^{-1} was assigned to the C=O stretching vibration of carboxylic acid groups, confirming the successful synthesis and purity of the intermediate TK-COOH. Concurrently, the O–H absorption band at 3400 cm^{-1} exhibited broadening, likely due to the overlapping contributions from carboxylic acid O–H groups. Additionally, alterations in the peak profile within the C–O region provided evidence for the grafting of sulfur-containing thioacetal moieties onto the APS sugar chain. In the spectrum of APS-TK-RAPA, the carboxylic acid C=O peak at 1688 cm^{-1} disappeared while a characteristic ester C=O absorption emerged at 1720 cm^{-1}. Meanwhile, the amide group absorption at 1642 cm^{-1} from the RAPA molecule was retained. These results indicated that esterification between APS-TK-COOH and RAPA has been successfully achieved, forming the desired product.

3.2 Preparation and characterization of HPPH@APS-TK-RAPA NP

The ATKR nanoparticle (ATKR NP) was obtained from APS-TK-RAPA via dialysis, whereas the self-assembly of HPPH and APS-TK-RAPA was conducted using the solvent evaporation technique, followed by filtration through a 0.22 μm membrane to yield the HPPH@ATKR nanoassembly (HPPH@ATKR NP).

The drug loading efficiency and encapsulation efficiency of HPPH, as determined by UV–Vis, was found to be 13.51% ± 0.45% and 85.3% ± 2.41%, respectively. This result suggested that the synthesized nanomaterials possess a favorable drug loading capacity (the standard curve for HPPH was showed in Fig. S1(b) in the ESM). DLS analysis revealed that the average particle sizes of ATKR NP and HPPH@ATKR NP in aqueous solution were 243.30 ± 3.18 nm (Fig. S2(a) in the ESM) and 170.10 ± 1.95 nm (Fig. 3(a)), respectively, both exhibiting unimodal size distributions. The polydispersity index (PDI) values were below 0.2, indicating uniform assembly and structural stability of the nanoparticles. Measurements of the particle size and zeta potential within 7 days confirmed the stability of ATKR NP and HPPH@ATKR NP

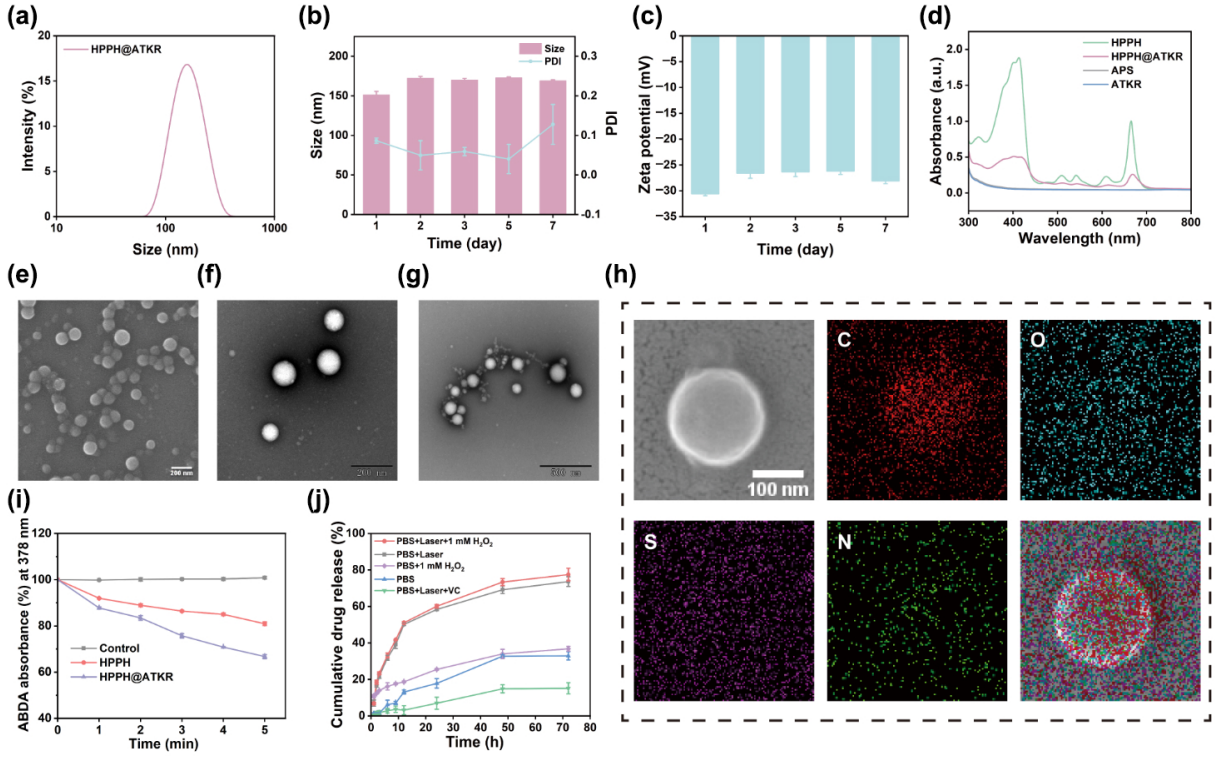

Figure 3 Characterization of HPPH@ATKR NP. (a) The hydrodynamic size of HPPH@ATKR via DLS. (b) Size and PDI stability and (c) zeta potential of HPPH@ATKR dispersed in water during one week. (d) The UV–Vis spectra of HPPH in DMSO, HPPH@ATKR in water, APS in water and ATKR in water. (e) SEM image (scale bar: 200 nm), (f) TEM image (scale bar: 200 nm) and (g) TEM image (scale bar: 500 nm) with H_2O_2 (100 μM) of HPPH@ATKR. (h) SEM mapping images of HPPH@ATKR indicated the distribution behaviors of C, O, N and S. (i) ABDA absorbance of the Control, HPPH, HPPH@ATKR groups (n = 3). (j) *In vitro* release pattern of HPPH from HPPH@ATKR in different H_2O_2 concentrations and light conditions (n = 3). Data represented as mean ± SD.

(Figs. 3(b) and 3(c), and Figs. S2(b) and S2(c) in the ESM). Furthermore, no significant variations in particle size or PDI were observed across different media (PBS, 1% NaCl, RPMI 1640) (Fig. S3 in the ESM), suggesting that HPPH@ATKR NP exhibits favorable adaptability under physiological conditions. The CMC, determined via a fluorescent probe method, was 57.54 μg/mL (Fig. S4 in the ESM), falling within the typical range for polymeric micelles (10–100 μg/mL). This indicates that ATKR NP can maintain its nanostructure under *in vivo* dilution, which is beneficial for enhancing drug delivery stability and circulation time. Ultraviolet–visible spectrum of HPPH@ATKR NP was almost overlapped with HPPH at 407 and 660 nm, confirming the successful encapsulation of HPPH (Fig. 3(d)).

TEM analysis reveals that APS exhibits a relatively loose and amorphous morphology, whereas the APS-TK-RAPA amphiphilic material demonstrates a comparatively dense structure with enhanced dispersibility (Figs. S5(a) and S5(b) in the ESM). In contrast, the initial self-assembly system of ATKR NP displays irregular dendritic aggregates distinct from the aforementioned structures (Fig. S5(c) in the ESM). This phenomenon is hypothesized to result from the aggregation of hydrophobic domains driven by amphiphilic molecules in the aqueous environment, coupled with insufficient coverage by hydrophilic segments. SEM (Fig. 3(e)) and TEM imaging (Fig. 3(f)) of HPPH@ATKR NP reveal regular, uniform spherical particles with well-defined edges, suggesting that the incorporation of hydrophobic HPPH further stabilizes the hydrophobic core of the ATKR system and facilitates the formation of structurally compact nanomedicine. Notably, upon the addition of 1 mM H_2O_2 to the medium (to facilitate accelerated release kinetics [32]), TEM images demonstrate significant morphological alterations (Fig. 3(g)): the initially spherical nanoparticles progressively disintegrate, forming beaded chain-like structures composed of connected particles and filamentous elements. This morphological transformation is attributed to the cleavage of TK bonds within the carrier under oxidative conditions, resulting in the removal of the hydrophilic shell, exposure of the hydrophobic core, and subsequent secondary aggregation. Additionally, some residual hydrophilic segments may extend to form filamentous connections during sample drying. Collectively, these findings indicate that HPPH@ATKR NP exhibit pronounced responsiveness to H_2O_2, undergoing structural reconfiguration under oxidative stress, thereby providing a mechanistic basis for drug release within the tumor microenvironment. Furthermore, energy dispersive X-ray (EDX) elemental mapping confirms the presence of carbon, oxygen, sulfur, and nitrogen elements (Fig. 3(h)), with sulfur specifically corresponding to the thioketal linkages.

3.3 *In vitro* ROS generation ability

The ROS generation capability of HPPH@ATKR NP under near-infrared (NIR) light irradiation was assessed utilizing the ABDA probe assay. UV–Vis spectra of ABDA-containing nanoparticles were recorded following exposure to a 660 nm laser at predetermined time intervals (Fig. S6 in the ESM). A progressive decrease in the absorption peaks corresponding to HPPH and HPPH@ATKR NP was observed with increasing irradiation duration, whereas the absorption peak of ABDA in the Control group remained largely unchanged. These findings indicate that

formulations containing HPPH effectively generate ROS, while ABDA and the irradiation conditions alone exert negligible influence on ROS production. As a scavenger primarily targeting singlet oxygen ($^1O_2$), ABDA exhibits a marked reduction in its characteristic absorption peak at 378 nm upon reaction with ROS [11]. Consequently, UV–Vis absorbance at 378 nm was further quantified after 5 min of laser irradiation (Fig. 3(i)). The absorbance in the Control group remained stable, whereas the values for HPPH and HPPH@ATKR NP decreased to 80.92% ± 0.81% and 66.73% ± 0.86%, respectively, confirming the efficient ROS generation by the drug-loaded nanoparticles under light exposure. This photosensitizing property is attributed to the HPPH molecule, which produces reactive singlet oxygen ($^1O_2$) upon NIR excitation. The generated ROS subsequently induce cleavage of TK bonds within the nanostructure, leading to its disruption and serving as a trigger for drug release. Moreover, the capacity for photosensitive ROS generation underpins the potential utility of this system in PDT applications. While trace amounts of other ROS may be produced, $^1O_2$ serves as the primary cytotoxic mediator responsible for the observed therapeutic efficacy.

3.4 Drug release performances

The *in vitro* release behavior of HPPH@ATKR NP demonstrated notable variations under different stimulation conditions (Fig. 3(j)). In PBS, the nanostructure remained relatively stable, exhibiting a cumulative drug release of only 32.97% ± 2.30%, indicative of a predominantly diffusion-controlled release mechanism. Upon the addition of 1 mM H_2O_2 to the medium (to facilitate accelerated release kinetics [33, 34]), the cumulative release modestly increased to 36.80% ± 1.33%. In addition, exposure to NIR light irradiation for 5 min (PBS + Laser group) markedly enhanced drug release, achieving a cumulative release of 73.65% ± 2.67% at 72 h. This enhancement is attributed to the generation of ROS by the photosensitizer under laser irradiation, which facilitates the cleavage of TK bonds. Given the covalent conjugation of RAPA via TK linkers, the RAPA release rate serves as a quantitative indicator of bond cleavage efficiency, as shown in Fig. S7 in the ESM. Consequently, the nanoassembly shell disintegrated, leading to accelerated drug release. The introduction of the ROS scavenger vitamin C (VC) in the PBS + Laser + VC group resulted in a significant reduction in release (15.16% ± 3.01%), thereby confirming the critical role of photosensitization-induced ROS in nanoparticle destabilization. The PBS + Laser + H_2O_2 group showed the most rapid release profile, with a cumulative release of 77.50% ± 3.46% at 72 h and an elevated initial release rate. This result demonstrates that the synergistic oxidative effect of H_2O_2 and photosensitization-generated ROS significantly accelerates the nanoparticle disintegration. Overall, these findings substantiate that APS-TK-RAPA possesses high ROS sensitivity. Notably, the near-complete drug release in the synergistic group suggests a highly efficient cleavage of TK linker, rendering it a promising candidate for on-demand drug release within the tumor microenvironment.

3.5 Cellular uptake efficiency and mechanism

To assess cellular uptake characteristics and intracellular localization of HPPH@ATKR NP, confocal microscopy was employed to observe the internalization of the formulation (red fluorescence) and its colocalization with lysosomes labeled by LysoTracker (green) (Fig. 4(a)). The findings demonstrated a marked increase in the red fluorescent signal corresponding to the formulation over time, reaching the maximum intensity at 4 h of incubation. This suggests that the nanosystem can be effectively internalized by cells and facilitate the gradual release of HPPH. However, compared with free HPPH molecules, the HPPH@ATKR NP group exhibited a slightly diminished fluorescent signal within the same timeframe (Figs. S8(a)–S8(c) in the ESM). This difference is likely attributable to differing uptake mechanisms: free HPPH molecules traverse the cell membrane rapidly via passive diffusion, whereas drug-loaded nanoplatforms are internalized mainly through endocytosis, resulting in a comparatively slower initial uptake rate. In addition, the hydrophilic shell of the nanoformulation may impede immediate interaction between HPPH and the cell membrane, contributing to the observed gradual increase in fluorescence as HPPH is released. Colocalization analysis revealed that the red fluorescence in the HPPH@ATKR NP group highly overlapped with the green lysosomal signal (Pearson's correlation coefficient, PCC = 0.69 ± 0.05), indicating significant accumulation within lysosomes (Fig. 4(b)). In contrast, free HPPH exhibited a diffuse cytoplasmic distribution with minimal lysosomal co-localization. These observations corroborate the proposed differences in uptake pathways between the two formulations. The distinct localization reflects the critical influence of the carrier structure on the drug's intracellular trafficking.

Importantly, the lysosomal accumulation of HPPH@ATKR NP may serve as a stable reservoir for subsequent photosensitizer activation and ROS generation, while laying a foundation for the controlled release of HPPH and RAPA after TK bond cleavage.

The cellular uptake efficiency of HPPH@ATKR NP was further evaluated using flow cytometry (Figs. 4(c) and 4(d)). The intracellular fluorescence intensity measurements corresponded well with fluorescence images, thereby confirming the stable internalization and effective drug delivery facilitated by the nanoparticle. Endocytosis inhibition assays (Figs. 4(e) and 4(f)) were conducted to elucidate the uptake mechanism. Free HPPH exhibited no significant change in cellular uptake upon treatment with cyclodextrin, chlorpromazine, or amiloride (Figs. S8(d) and S8(e) in the ESM), suggesting that its cellular entry occurs primarily via passive diffusion across the plasma membrane. Conversely, HPPH@ATKR NP demonstrated a marked decrease in fluorescence intensity following cyclodextrin treatment, indicating that lipid raft-mediated endocytosis constitutes the principal internalization pathway [35]. Additionally, partial inhibition observed with chlorpromazine and amiloride treatments implied that clathrin-mediated endocytosis and macropinocytosis serve as secondary uptake routes [36, 37]. The resultant nanostructures, approximately 150–200 nm in diameter, are suitably sized for endocytic uptake, facilitating energy-dependent intracellular drug delivery.

3.6 Induction of intracellular ROS

The intracellular ROS level directly affects the PDT effect [38]. We investigated the intracellular ROS generation capacity using a fluorescence probe DCFH-DA. As illustrated in Fig. 5(a), both the Control and Control + Laser groups exhibited almost no fluorescence, indicating that laser irradiation alone does not induce ROS production. The HPPH group demonstrated only faint green fluorescence, whereas the HPPH + Laser group showed a marked increase in ROS levels following light exposure, confirming the effective activation of HPPH under NIR light excitation. In the HPPH@ATKR NP group, ROS levels remained low without light,

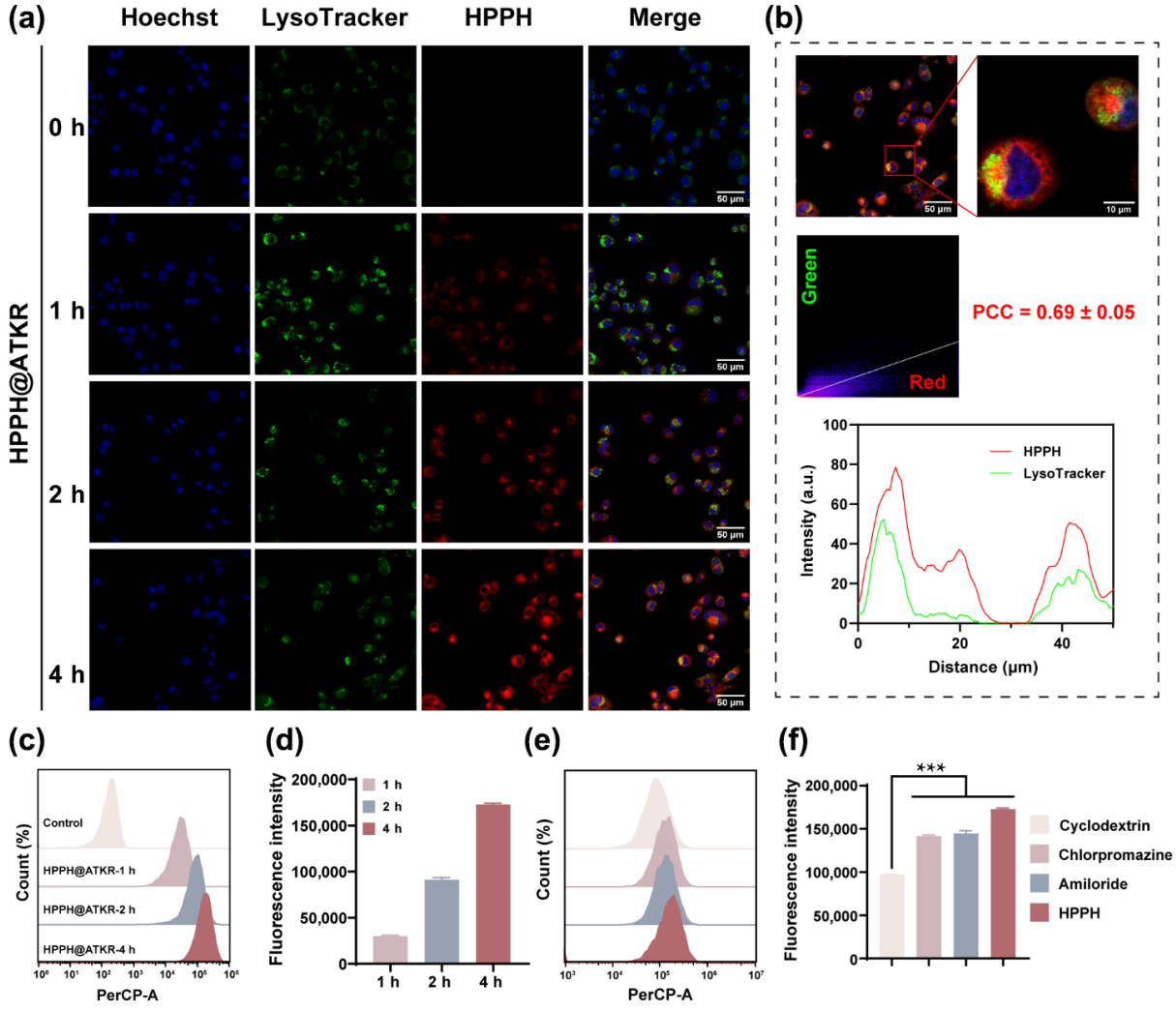

Figure 4 The cellular uptake ability of 4T1 cells. (a) The fluorescence images incubated with HPPH@ATKR from 0 to 4 h (blue channel: Hoechst, green channel: LysoTracker, red channel: HPPH, scale bars: 50 μm) of cellular uptake ability. (b) Fluorescence co-localization of HPPH (red) and lysosomes labeled by LysoTracker (green). The scale bars were 50 μm in the merged image and 10 μm in the enlarged image. (c) Flow cytometry analysis and (d) quantitative analysis of fluorescence intensity of cellular uptake ability ($n = 3$). (e) The flow cytometry analysis and (f) quantitative analysis of fluorescence intensity of cellular uptake ability after the addition of uptake inhibitors ($n = 3$). Data represented as mean ± SD, $^{*}P < 0.05$, $^{**}P < 0.01$, and $^{***}P < 0.001$.

corroborating the stability of the drug-loaded nanostructure and the absence of premature HPPH release. Importantly, upon irradiation, the HPPH@ATKR NP exhibited the most intense green fluorescence signal, suggesting that laser activation not only facilitates HPPH release from the nanoparticle but may also induce cleavage of thioketal bonds via ROS, thereby accelerating drug release. This process effectively enhances ROS generation and improves PDT efficacy. These findings substantiate the photosensitive responsiveness and synergistic therapeutic potential of HPPH@ATKR NP. Quantitative analysis of intracellular ROS levels, as determined by flow cytometry (Figs. 5(b) and 5(c)), were consistent with the fluorescence imaging results, further validating that laser-activated drug-loaded nanoplatforms promote ROS production and possess significant PDT capabilities. To further identify the specific ROS subtypes, the singlet oxygen sensor green (SOSG) probe was employed. The results confirmed that $^{1}O_2$ is the predominant reactive species generated via the Type II photochemical mechanism (Fig. S9 in the ESM).

3.7 *In vitro* cytotoxicity assay and cell apoptosis analysis

The *in vitro* cytotoxic effects of HPPH, RAPA+HPPH and HPPH@ATKR were evaluated before and after exposure to 660 nm laser irradiation using the CCK-8 assay. As illustrated in Fig. 5(d), after 24 h of incubation, the HPPH group exhibited minimal cytotoxicity toward 4T1 cells, indicating that HPPH alone does not exert significant toxicity in the absence of laser activation. In comparison to the HPPH group, the HPPH@ATKR group showed increased cellular inhibition, suggesting that the incorporation of the carrier enhances the cytotoxic potential of HPPH to some extent. Upon irradiation with a 660 nm laser at an intensity of 200 mW/cm^2 for 5 min, the HPPH@ATKR group demonstrated the most prominent cytotoxic effect (Fig. 5(e)). This synergistic therapeutic outcome is attributed to the activation of the photosensitizer HPPH by NIR laser irradiation, which induces the generation of ROS. The ROS subsequently facilitate the cleavage of the TK bond, leading to nanosystem disassembly and the rapid release of RAPA. Furthermore, the presence of RAPA significantly enhances the efficacy of PDT.

The apoptosis of cells following treatment in each experimental group was assessed via flow cytometry (Figs. 5(f) and 5(g)).

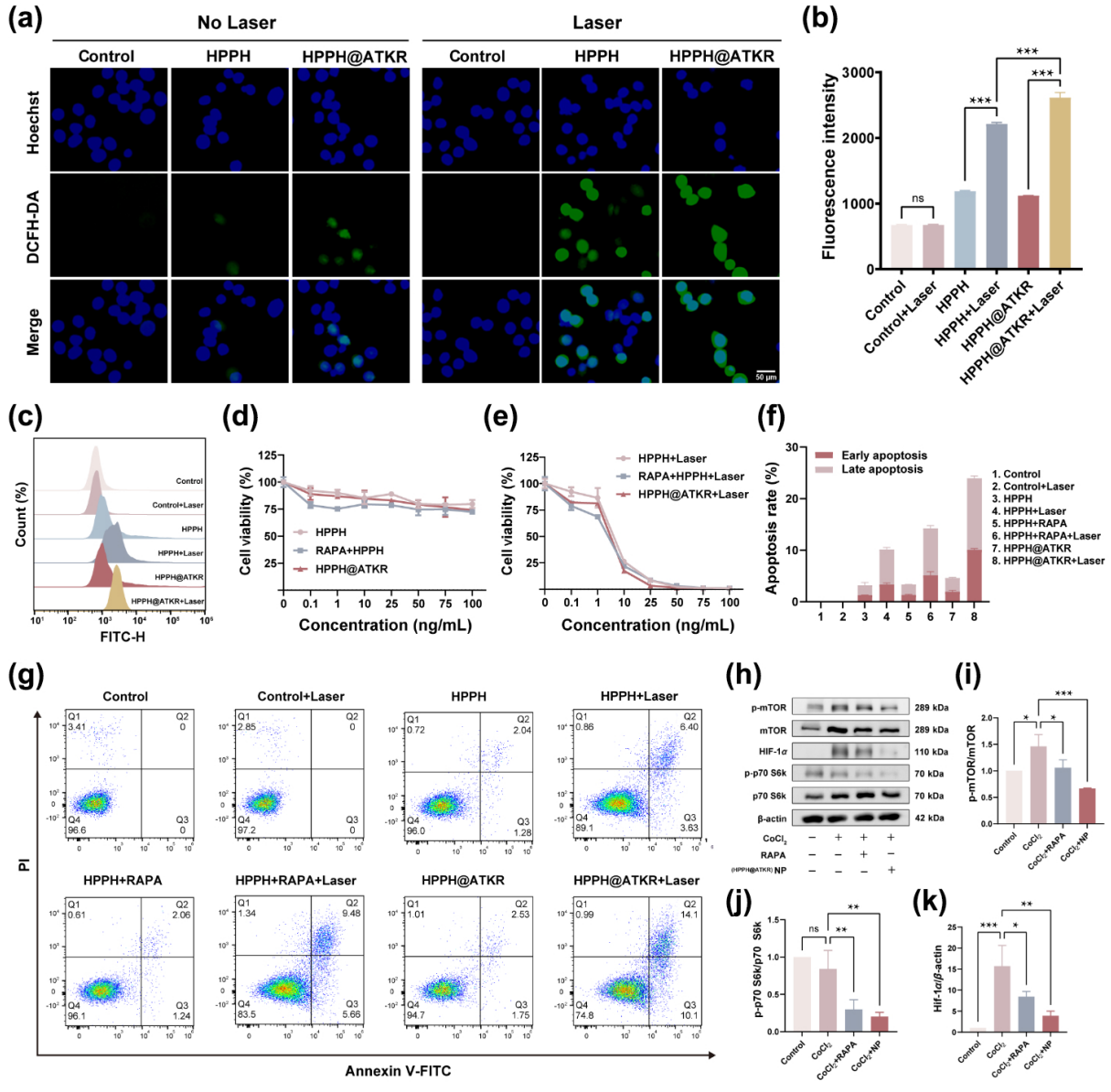

Figure 5 Intracellular ROS generation, cytotoxicity and apoptosis performance. (a) Fluorescence images (blue channel: Hoechst, green channel: DCFH-DA, scale bar: 50 μm), (b) flow cytometry quantitative analysis and (c) histogram of intracellular ROS generation (n = 3). (d) Viability of 4T1 cells after the treatment of HPPH, RAPA+HPPH and HPPH@ATKR NP (n = 3). (e) Viability of 4T1 cells after the treatment of HPPH, RAPA+HPPH and HPPH@ATKR NP with 660 nm laser irradiation (n = 3). (f) Quantitative analysis and (g) flow cytometry analysis of apoptosis rate induced by different treatments (n = 3). (h) Western blot analysis of mTOR, p-mTOR, HIF-1α, p70 S6k, and p-p70 S6k in 4T1 cells. Statistical analysis of (i) p-mTOR/mTOR, (j) p-p70 S6k/p70 S6k, and (k) HIF-1α after exposure to $CoCl_2$, $CoCl_2$+RAPA, $CoCl_2$+HPPH@ATKR NP (n = 3). Data represented as mean ± SD, $^*P < 0.05$, $^{**}P < 0.01$, and $^{***}P < 0.001$.

Minimal apoptosis was observed in both the Control and Control + Laser groups, with total apoptosis rates below 1%. Under 660 nm laser irradiation, the apoptosis rates in the HPPH group, RAPA + HPPH group, and HPPH@ATKR group were all elevated compared to no laser groups. The HPPH + Laser group exhibited a total apoptosis rate of 10.14% ± 0.10%, suggesting that the photosensitizer HPPH can elicit a PDT effect after activation. The RAPA + HPPH + Laser group demonstrated an increased total apoptosis rate of 14.22% ± 1.27% relative to the HPPH + Laser group, indicating the contribution to cell apoptosis after adding RAPA. Notably, the HPPH@ATKR + Laser group achieved the highest cell death rate, with total apoptosis and necrosis reaching 23.93% ± 0.75% (comprising 10.06% ± 0.26% early apoptosis and 13.87% ± 0.49% late apoptosis), which significantly surpassed other groups and aligned with *in vitro* cytotoxicity findings. These results imply that HPPH@ATKR NP not only facilitates the release of HPPH to generate ROS upon light activation but also promotes RAPA release, thereby producing a synergistic cytotoxic effect through combined PDT and chemotherapy, effectively inducing tumor cell apoptosis.

To further elucidate the molecular mechanism by which RAPA enhances therapeutic efficacy, the mTOR-HIF-1α signaling axis was investigated via Western blot under $CoCl_2$-induced hypoxia (Figs. 5(h)–5(k)). The results showed that HPPH@ATKR NP significantly downregulated the expression of p-mTOR and p-p70 S6K, effectively inhibiting the compensatory activation of the mTOR pathway. Concurrently, a marked reduction in HIF-1α levels was observed, providing direct evidence that the delivered

RAPA ameliorates the hypoxic microenvironment by suppressing the mTOR-HIF-1α axis, thereby sensitizing tumor cells to PDT-induced apoptosis.

3.8 Induction of ICD and DC maturation *in vitro*

ICD is characteristically accompanied by the translocation of CRT to the cell surface, the release of HMGB1, and the substantial secretion of extracellular ATP, all of which play critical roles in activating dendritic cells and eliciting anti-tumor immune responses [39, 40]. To assess the capacity of 4T1 cells to induce ICD under various treatment conditions, this study systematically detected the levels of membrane-bound CRT, intracellular HMGB1 and ATP. Immunofluorescence analysis revealed that the HPPH@ATKR combined with laser irradiation group exhibited the most intense green fluorescence on the cell membrane, indicative of pronounced CRT externalization. Concurrently, this group demonstrated the weakest nuclear red fluorescence of HMGB1, suggesting extensive extracellular release of this protein. In contrast, treatment with HPPH alone or in the absence of laser exposure did not result in significant CRT translocation or HMGB1 release, implying that the HPPH@ATKR NP require laser activation to effectively induce ICD. Furthermore, quantification of intracellular ATP levels showed the lowest concentration in the HPPH@ATKR + Laser group, indicating enhanced extracellular ATP release and potentiation of immune stimulatory signals (Figs. 6(a) and 6(b)). These findings collectively confirm that HPPH@ATKR, upon laser activation, robustly triggers ICD through the promotion of CRT exposure, HMGB1 release, and ATP secretion, thereby markedly

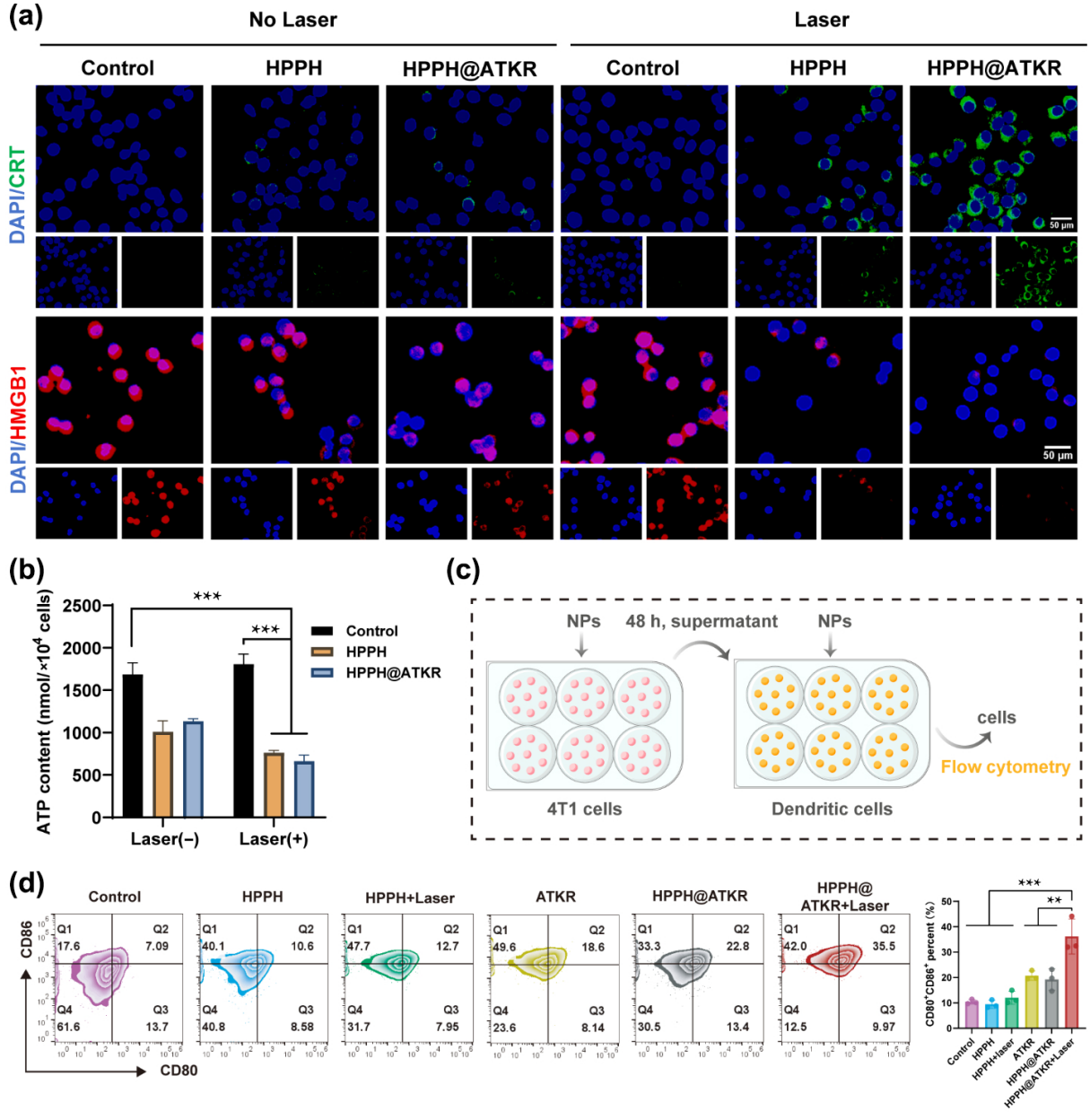

Figure 6 Evaluation of ICD induction and the ability to promote dendritic cell maturation. (a) CRT exposure and HMGB1 release in 4T1 cells with different treatments (scale bars: 50 μm). (b) ATP secretion from different formulation-treated 4T1 cells (n = 3). (c) Schematic illustration of the coincubation experiment of 4T1 and DC2.4 cells. NPs, nanoparticles. (d) The proportions of mature DCs ($CD80^+CD86^+$) at DC2.4 cells with different treatments by flow cytometric analysis (n = 3). Data represented as mean ± SD, $^*P < 0.05$, $^{**}P < 0.01$, and $^{***}P < 0.001$.

augmenting the immunotherapeutic efficacy of the photosensitizer HPPH.

To further assess the immune activation potential, culture supernatants from 4T1 cells subjected to various treatments were collected and subsequently incubated with immature DC2.4 cells [41]. The expression levels of mature DC markers ($CD80^+CD86^+$) were then evaluated via flow cytometry (Fig. 6(c)). As shown in Fig. 6(d), the group treated with HPPH@ATKR + Laser exhibited the highest proportion of mature DCs at 36.16% ± 6.87%, significantly surpassing both the HPPH + Laser group (12.00% ± 2.59%) and the ATKR group (20.69% ± 1.85%). Notably, the ATKR group alone induced higher DC maturation compared to the HPPH + Laser group, which can be attributed to the intrinsic adjuvant effect of APS. Previous studies have confirmed that APS directly stimulates DC differentiation and maturation by acting as a bioactive scaffold [25, 26]. Conversely, treatments without laser exposure demonstrated a diminished capacity to induce DC maturation, while the Control group showed negligible effects. This trend was especially pronounced in the CD80 and CD86 double-positive quadrant, suggesting that the supernatant derived from laser-activated HPPH@ATKR NP contained a greater concentration of potent immune-stimulating factors. In conclusion, HPPH@ATKR NP effectively activate anti-tumor immune responses through a dual-mechanism: the induction of ICD-

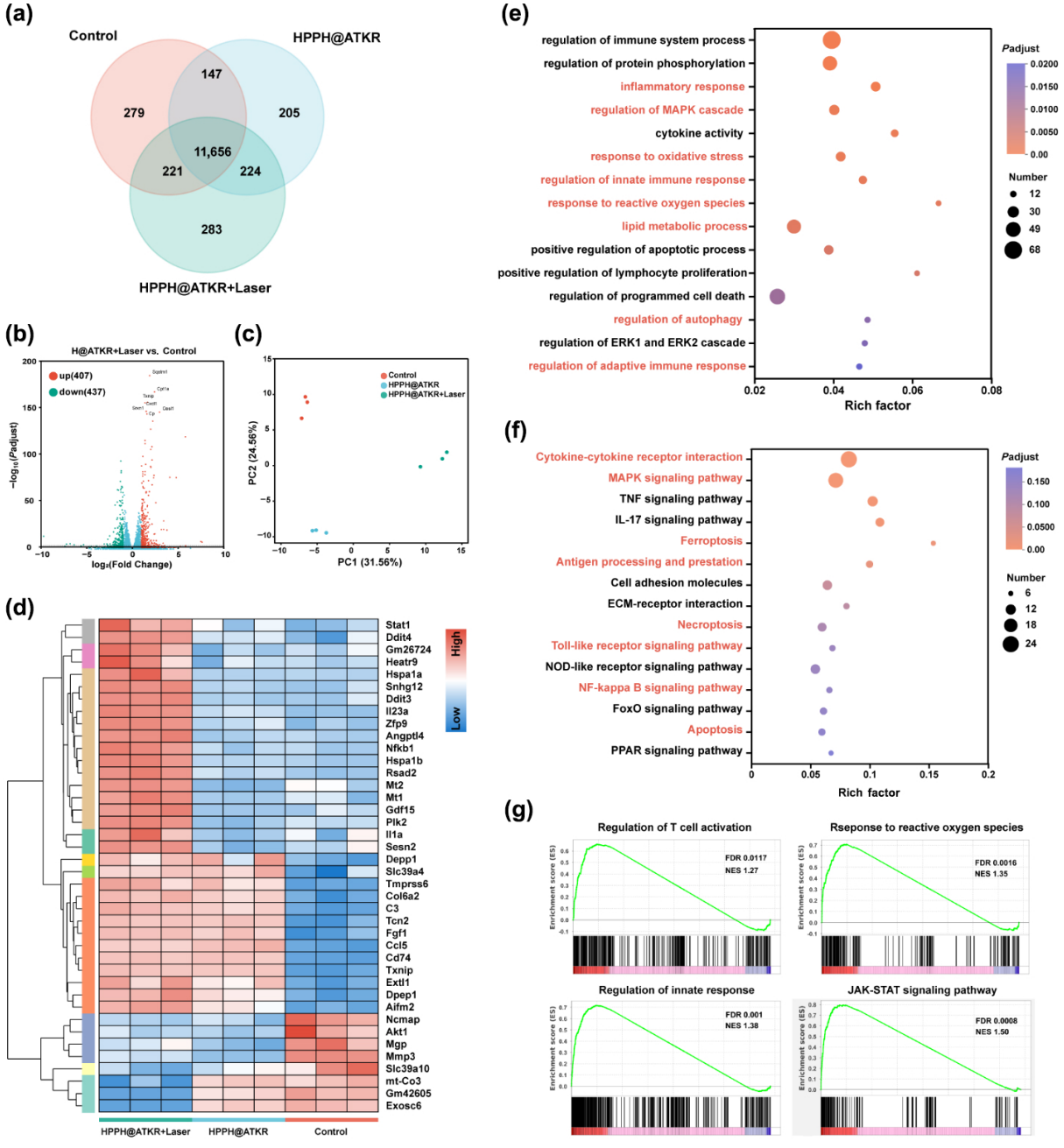

Figure 7 Transcriptomic analysis. (a) Venn picture indicated the intersection of gene expression number in 4T1 cells pretreated with PBS (Control), HPPH@ATKR, and HPPH@ATKR + Laser. (b) Volcano plot exhibited the differentially expressed genes between HPPH@ATKR + Laser and PBS (Control) treatment. (c) PCA analysis of different treatments. (d) Heat map of some differentially expressed genes. (e) Diagram of GO enrichment analysis and (f) KEGG enrichment analysis between HPPH@ATKR + Laser and Control groups. (g) Representative gene set enrichment mountain plots of HPPH@ATKR + Laser/Control.

associated DAMPs by PDT and the inherent immunomodulatory activity of the APS carrier. This provides a robust foundation for their application in tumor immunotherapy.

3.9 RNA-sequencing analysis

Owing to the transcriptome sequencing on 4T1 cells exposed to different treatments, the mechanism underlying the enhanced PDT efficiency of HPPH@ATKR was analyzed by comparing gene expression among the Control, HPPH@ATKR, and HPPH@ATKR + Laser groups. This grouping strategy was specifically designed to capture the holistic biological transition of the integrated nano-platform from a dormant state to a fully activated state, highlighting the multi-pathway synergy among HPPH-mediated PDT, RAPA-sensitization, and APS-adjuvant effects. Among all detected genes, both HPPH@ATKR and its laser-activated form distinctly reshaped cellular transcriptional profiles (Fig. 7(a)). Compared with the control, HPPH@ATKR treatment alone induced marked transcriptional alterations, indicating intrinsic bioactivity of the formulation. Laser activation further intensified these changes, reflecting additional modulation triggered by the photoexcited sensitizer (Fig. 7(b), and Fig. S10(a) in the ESM). In addition, we examined the intersection of differentially expressed genes between HPPH@ATKR + Laser/Control and HPPH@ATKR/Control (Fig. S10(b) in the ESM). These findings suggested that the HPPH@ATKR formulation alone could elicit differential expression in a subset of genes, whereas the application of light further modulated an additional distinct set of genes. Principal component analysis (PCA) revealed pronounced distinctions among the Control, HPPH@ATKR, and HPPH@ATKR + Laser groups (Fig. 7(c)).

Subsequently, we screened genes related to key pathways of interest and some of the corresponding results were displayed by heat maps (Fig. 7(d)). Additionally, Gene Ontology (GO) and Kyoto Encyclopedia of Genes and Genomes (KEGG) analyses revealed that differential genes under laser-activated treatment were mainly enriched in oxidative stress response, mitogen-activated protein kinase (MAPK)/extracellular signal-regulated kinase (ERK) signaling, and immune-related processes, confirming that HPPH@ATKR under laser activation triggered oxidative stress-associated transcriptional reprogramming and immune signal activation (Figs. 7(e) and 7(f), and Figs. S11(a), S11(b), S12(a), and S12(b) in the ESM). Furthermore, Gene Set Enrichment Analysis (GSEA) indicated positive enrichment of response to reactive oxygen species, Janus kinase-signal transducer and activator of transcription (JAK-STAT) signaling pathway and immune activation pathways after laser irradiation (Fig. 7(g), and Figs. S13(a) and S13(b) in the ESM). These transcriptomic findings are further supported by the molecular downregulation of the mTOR-HIF-1α axis, confirming the targeted disruption of tumor oxidative stress adaptation. Collectively, these results suggest that the enhanced PDT efficiency of HPPH@ATKR with laser activation originates from elevated ROS generation and stimulation of immune responses at the transcriptomic level.

3.10 Hemolysis assay

The blood compatibility of HPPH@ATKR NP was assessed using a hemolysis assay (Fig. S14 in the ESM). Deionized distilled water (dd H_2O) served as the positive control and exhibited pronounced red hemolysis, indicative of extensive erythrocyte membrane disruption. In contrast, the saline group, employed as the negative control, showed no hemolytic activity. Across a concentration range of 10 to 100 μg/mL, HPPH@ATKR NP did not produce a visibly red supernatant, suggesting favorable blood compatibility. Quantitative analysis revealed that the hemolysis rates at all tested concentrations remained below 5% (the established safety threshold) with a slight concentration-dependent increase observed [42]. These findings indicate that HPPH@ATKR NP does not induce significant erythrocyte lysis under *in vitro* conditions and exhibits excellent biocompatibility, supporting its potential utility for subsequent *in vivo* drug delivery applications.

3.11 Anti-tumor effect

Given the potent *in vitro* anti-tumor efficacy of HPPH@ATKR nanoparticles and the capacity to induce DAMPs release, an orthotopic solid tumor model was established by implanting 4T1 cells into the mammary fat pad of BALB/C mice to facilitate *in vivo* investigations of anti-tumor efficacy. Treatment commenced once tumor volumes reached approximately 100 mm^3 [43]. Experimental groups included Control, Control + Laser, HPPH + Laser, RAPA, RAPA + HPPH + Laser, ATKR, HPPH@ATKR, and HPPH@ATKR + Laser (660 nm, 200 mW/cm^2, 5 min; n = 6 per group, determined by G*Power software (version 3.1.9.7) analysis based on a pilot study) (Fig. 8(a)). The findings revealed that free HPPH + Laser group produced only a moderate tumor growth inhibition. In contrast, the HPPH@ATKR + Laser group exhibited the most pronounced tumor suppression, achieving a tumor inhibition rate of 71.82% ± 9.75%, significantly reduced tumor volume, and a sustained decrease in tumor growth rate (Figs. 8(b)–8(e)). Histological analyses, including H&E and TUNEL staining, demonstrated marked nuclear condensation, chromatin margination, and extensive apoptotic signals within tumor cells of the HPPH@ATKR + Laser group (Fig. 8(f)). Meanwhile, throughout the treatment period, the body weight of the mice remained stable (Fig. S15(a) in the ESM), and no significant alterations were observed in major organ indices (heart, liver, spleen, lung, and kidney) (Fig. S15(b) in the ESM). Furthermore, H&E staining revealed no evident tissue damage in these organs (Fig. S15(c) in the ESM), indicating favorable biocompatibility and safety of the nanoplatform. The above results substantiate that the HPPH@ATKR nanoplatform, upon light activation, synergistically utilizes the sensitization effect of RAPA and the immune adjuvant effect of APS to elicit a robust anti-tumor immune response, thereby demonstrating excellent therapeutic effects. Notably, supplementary investigations with an optimized dosing regimen (3 mg/kg, 4 injections) demonstrated a more sustained tumor suppression with a higher inhibition rate of 89.02% ± 3.29% and no observed systemic toxicity (Fig. S16 in the ESM), suggesting the broad therapeutic window and potency of this integrated system.

3.12 Enhanced photoimmunological response by HPPH@ATKR NP

To understand the underlying mechanism responsible for the enhanced photodynamic immunotherapy mediated by HPPH@ATKR NP, *ex vivo* immunofluorescence staining and flow cytometry analyses were conducted to assess antitumor immune responses. Further mechanistic investigations revealed a significant downregulation of HIF-1α expression in tumor tissues of mice treated with the HPPH@ATKR NP combined with laser irradiation (Figs. 9(a) and 9(b)). Previous studies have established that persistent overexpression of HIF-1α constitutes a principal

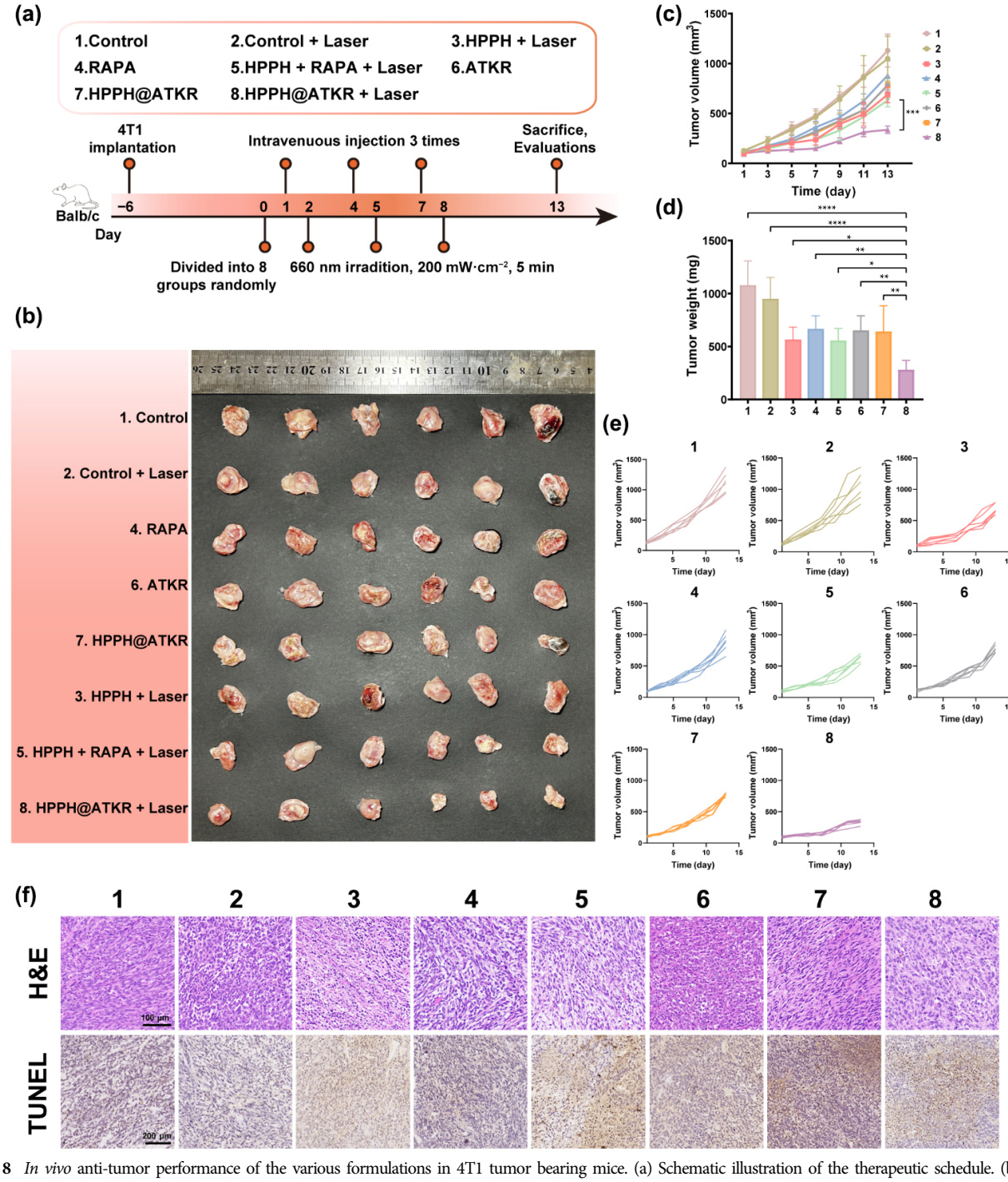

Figure 8 *In vivo* anti-tumor performance of the various formulations in 4T1 tumor bearing mice. (a) Schematic illustration of the therapeutic schedule. (b) Digital photograph of the excised tumors at the end of treatment. (c) Tumor volume among different groups (n = 6). (d) Tumor weight after treatment with different formulations (n = 6). (e) Tumor growth curve with different treatments over a period of 13 days. (f) H&E (scale bar: 100 μm) and TUNEL staining (scale bar: 200 μm) results of the tumor sections at the end of treatment in eight groups. Data represented as mean ± SD, $^{*}P < 0.05$, $^{**}P < 0.01$, $^{***}P < 0.001$ and $^{****}P < 0.0001$.

mechanism causing resistance to the photosensitizer HPPH, as it enhances tumor cell adaptation to hypoxic environment, suppresses ROS generation, and diminishes photodynamic therapy efficacy [44]. In this study, we found that the incorporation of RAPA markedly inhibited HIF-1α expression, thereby mitigating tumor hypoxia tolerance and consequently augmenting the laser sensitivity and cytotoxic effects of HPPH. Meanwhile, immunofluorescence staining demonstrated increased CRT exposure on the tumor cell membrane and a pronounced reduction in HMGB1 signals within this treatment group, indicating successful induction of ICD by HPPH in synergy with RAPA (Fig. 9(c)). It is well known that DAMPs released during ICD, including CRT and HMGB1, function as "eat me" and "danger" signals, can be recognized and internalized by DCs, thereby promoting DC maturation and antigen presentation [45]. It is a critical process for initiating anti-tumor immune responses [46].

Enhanced immunogenicity induced by PDT, tumor hypoxia alleviated through RAPA-mediated metabolic modulation, and

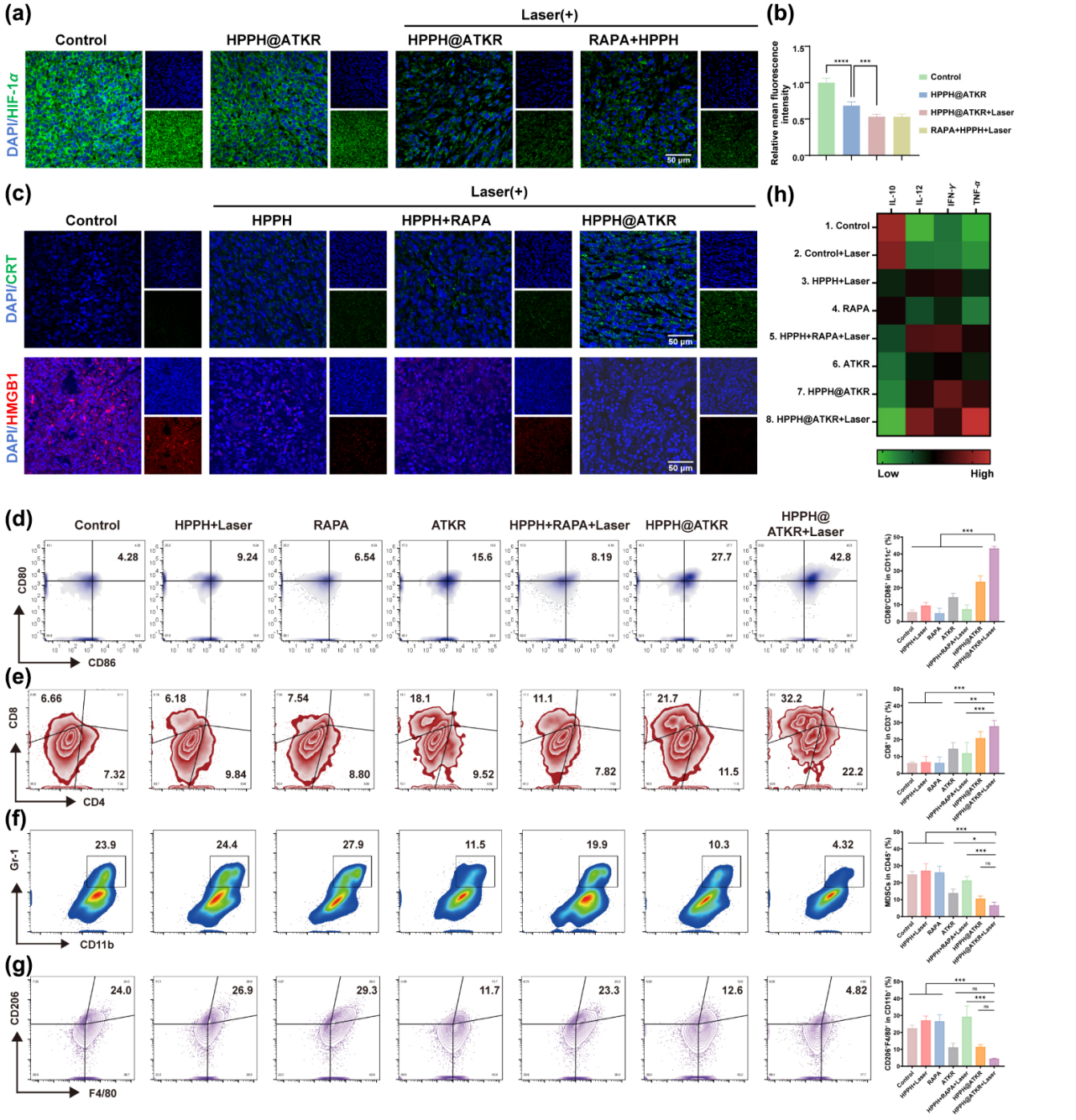

Figure 9 *In vivo* anti-tumor photoimmunological response. (a) Immune-fluorescence imaging and (b) quantitative analysis of the situation of hypoxia in 4T1 tumors (scale bar: 50 μm, n = 5). (c) Fluorescent imaging of CRT exposed and HMGB1 release in tumor tissues (scale bars: 50 μm). (d) Flow cytometry analysis of mature dendritic cells in DLNs, (e) $CD4^+/CD8^+$ T lymphocytes in tumors, (f) MDSCs in tumors, and (g) M2 macrophages in tumors after different treatments (n = 4). (h) ELISA analysis of the levels of inflammatory cytokines TNF-α, IFN-γ, IL-10, and IL-12 in tumors (n = 3). Data represented as mean ± SD, $^*P < 0.05$, $^{**}P < 0.01$, $^{***}P < 0.001$, and $^{****}P < 0.0001$.

immune activation potentiated by APS adjuvanticity collectively established the cooperative mechanism of HPPH@ATKR-based therapy to promote DC maturation and T-cell activation. Immune cells in tumors and tumor-DLNs from treated BALB/c 4T1 tumor-bearing mice were comprehensively analyzed by flow cytometry. The release of DAMPs such as HMGB1 and ATP after HPPH@ATKR + Laser treatment fueled DC maturation and antigen presentation. As shown in Fig. 9(d), the ratio of $CD80^+CD86^+$ DCs in DLNs reached 43.28% ± 1.14%, surpassing that of other groups, indicating enhanced immunogenicity and adjuvant activity of APS. The proportion of $CD8^+$ T cells within tumors also increased markedly in the HPPH@ATKR + Laser group, exhibiting a favorable systemic immune activation (Fig. 9(e)). APS could activate the Nrf2/HO-1 pathway to promote an anti-inflammatory immune milieu by reducing myeloid-derived suppressor cell (MDSC) activity and relieving immunosuppression [37]. Consistently, the percentage of $CD11b^+Gr\text{-}1^+$ MDSCs in tumors decreased to 7.80% ± 3.56% compared with 24.92% ± 1.72% in Control, confirming that the combination of HPPH@ATKR with irradiation effectively reduced

immunosuppressive cell accumulation (Fig. 9(f)). Moreover, the ratio of $CD206^{+}F4/80^{+}$ macrophages declined significantly, suggesting repolarization from the M2 to M1 phenotype (Fig. 9(g)). These results demonstrate that HPPH@ATKR + Laser effectively enhanced immunogenicity, strengthened immune activation, and alleviated tumor immunosuppression. Cytokine analysis further confirmed the enhanced immune activation. The proinflammatory cytokines tumor necrosis factor-alpha (TNF-α), interferon-gamma (IFN-γ), and interleukin-12 (IL-12) were significantly elevated, whereas the immunosuppressive cytokine IL-10 was markedly reduced in the HPPH@ATKR + Laser group (Fig. 9(h) and Fig. S17 in the ESM). These results further verified that the triple combination under laser irradiation efficiently remodeled the tumor immune microenvironment, establishing a proinflammatory and immune-active state conducive to effective antitumor immunity.

4 Conclusions

In conclusion, we have successfully developed a biocompatible and ROS-responsive nanoplatform (HPPH@ATKR) based on the clinical-proven and "Qi-tonifying" herb APS, which enables the co-delivery of the pharmacological sensitizer RAPA and the photosensitizer HPPH to enhance the efficacy of PDT alongside the anti-tumor immune response. This active bioactive nanosystem is characterized by uniform size and morphology, excellent colloidal stability, high drug-loading efficiency, and intelligent responsive drug release capabilities. Our research demonstrates that under NIR laser irradiation, the activated HPPH generates substantial ROS levels, triggering the cleavage of the TK bond and enabling targeted release of both HPPH and RAPA at the tumor site. RAPA improves the hypoxic tumor microenvironment by inhibiting the mTOR signaling pathway to downregulate HIF-1α expression, thereby significantly sensitizing HPPH-mediated PDT. Furthermore, as an immune adjuvant, APS can activate DCs, promote their maturation, and increase the efficiency of antigen uptake. Therefore, the biocompatible self-assembled drug delivery system HPPH@ATKR proposed in our study, through the synergistic interplay of HPPH, RAPA, and APS, presents a scientifically robust and highly promising anti-tumor therapeutic approach. This strategy leveraging the clinical translation potential of APS is expected to achieve a favorable synergy between photodynamic therapy and immunotherapy in cancer treatment.

Electronic Supplementary Material: Supplementary material (linear correlation of RAPA and HPPH against its corresponding concentrations, characterization of ATKR NP, the physiological medium stability of HPPH@ATKR NP, CMC value constituted by ATKR using pyrene probe, TEM images of APS, APS-TK-RAPA material and ATKR NP, the UV–Vis absorption spectra of ABDA, *in vitro* release pattern of RAPA from HPPH@ATKR, the cellular uptake ability of 4T1 cells with free HPPH, SOSG-based flow cytometry analysis and quantitative analysis for singlet oxygen detection, Venn plot, volcano diagram, GO enrichment analysis, KEGG enrichment analysis, GSEA multiple gene sets bubble plots, hemolysis image and hemolysis rate, biological safety evaluation to mice, *in vivo* anti-tumor performance of the various formulations in 4T1 tumor bearing mice at an increased administration dosage, enzyme-linked immunosorbent assay (ELISA) quantitative analysis of the levels of inflammatory cytokines TNF-α, IFN-γ, IL-10 and IL-12 in tumors) is available in the online version of this article at https://doi.org/10.26599/NR.2026.94908620.

Data availability

All data needed to support the conclusions in the paper are presented in the manuscript and the Electronic Supplementary Material. Raw transcriptome sequencing data are stored in the Sequence Read Archive (SRA, accession number: PRJNA1438704).

Acknowledgements

This work is granted by Key project at central government level: CAMS Innovation Fund for Medical Sciences (CIFMS, No. 2022-I2M-1-018), the National Natural Science Foundation of China (No. 82304733), the National Administration of Traditional Chinese Medicine Young Qihuang Scholar Project (2025), Jilin Province Science and Technology Development Program (No. 20260204103YY), and Natural Science Foundation of Jilin Province (No. YDZJ202501ZYTS701).

Declaration of competing interest

All the contributing authors report no conflict of interests in this work.

Author contribution statement

C. J. Z.: Writing – original draft, conceptualization, methodology, investigation, data curation. Y. Z.: Writing – original draft, conceptualization, validation, data curation, visualization. X. R. B.: Resources, investigation, methodology, data curation. H. X. G.: Formal analysis, methodology, data curation. Z. W.: Methodology, investigation, visualization. W. W. Z.: Resources, investigation. J. H. H.: Resources, investigation. T. F. J.: Writing – review & editing, validation, project administration, conceptualization. Z. Q. D.: Validation, funding acquisition, project administration, supervision.

Informed consent

Not applicable.

Ethics statement

This study involving animals was approved by the ethics committee of the Institute of Medicinal Plant Development (No. SLXD‑20241205019). All animal husbandry and experiments were conducted in strict accordance with the regulations for the management and use of laboratory animals.

Use of AI statement

None.

References

[1] Long, Y. Y.; Li, C. X.; Zhu, B. Y. Circ_0008068 facilitates the oral squamous cell carcinoma development by microRNA-153-3p/acylgycerol kinase (AGK) axis. *Bioengineered* **2022**, *13*, 13055–13069.

[2] Wang, L.; Du, L.; Xiong, X.; Lin, Y. S.; Zhu, J. L.; Yao, Z. M.; Wang, S. H.; Guo, Y.; Chen, Y. P.; Geary, K. et al. Repurposing

dextromethorphan and metformin for treating nicotine-induced cancer by directly targeting CHRNA7 to inhibit JAK2/STAT3/SOX2 signaling. *Oncogene* **2021**, *40*, 1974–1987.

[3] Chong, C. Y.; Goh, M. S.; Porceddu, S. V.; Rischin, D.; Lim, A. M. The current treatment landscape of cutaneous squamous cell carcinoma. *Am. J. Clin. Dermatol.* **2023**, *24*, 25–40.

[4] Mosaddad, S. A.; Namanloo, R. A.; Aghili, S. S.; Maskani, P.; Alam, M.; Abbasi, K.; Nouri, F.; Tahmasebi, E.; Yazdanian, M.; Tebyaniyan, H. Photodynamic therapy in oral cancer: A review of clinical studies. *Med. Oncol.* **2023**, *40*, 91.

[5] Chen, H. H.; Li, H. L.; Li, H. J.; Zhang, Z. Umbrella review of photodynamic therapy for cancer: Efficacy, safety, and clinical applications. *Front. Oncol.* **2025**, *15*, 1528314.

[6] Sahovaler, A.; Valic, M. S.; Townson, J. L.; Chan, H. H. L.; Zheng, M.; Tzelnick, S.; Mondello, T.; Pener-Tessler, A.; Eu, D.; El-Sayes, A. et al. Nanoparticle-mediated photodynamic therapy as a method to ablate oral cavity squamous cell carcinoma in preclinical models. *Cancer Res. Commun.* **2024**, *4*, 796–810.

[7] Li, Y. S.; Li, Y. Y.; He, G.; Li, X. X.; Ding, R.; Yan, R. H.; Lin, J.; Huang, P. Activatable enzymatic nanoplatform incorporated into microneedle patch for relieving tumor hypoxia augmented photodynamic therapy. *Adv. Mater.* **2025**, *37*, 2504258.

[8] Wang, H.; Lu, X. H.; Fan, J.; Yang, C. P.; Zhu, H. Y.; Liu, J. B.; Ding, B. Q. A carrier-free DNA nanoplatform for efficient three-in-one tumor therapy *in vivo*. *Nano Today* **2025**, *62*, 102734.

[9] Chen, L.; Zhang, X.; Cao, Q. Q.; Wu, Y. Q.; Zhang, T.; Tong, H.; Wang, X.; Yang, J. Development and application of a physiologically based pharmacokinetic model for HPPH in rats and extrapolate to humans. *Eur. J. Pharm. Sci.* **2019**, *129*, 68–78.

[10] Krishna, K. V.; Saha, R. N.; Puri, A.; Viard, M.; Shapiro, B. A.; Dubey, S. K. Pre-clinical compartmental pharmacokinetic modeling of 2-[1-hexyloxyethyl]-2-devinyl pyropheophorbide-a (HPPH) as a photosensitizer in rat plasma by validated HPLC method. *Photochem. Photobiol. Sci.* **2019**, *18*, 1056–1063.

[11] Hua, X. W.; Bao, Y. W.; Zeng, J.; Wu, F. G. Ultrasmall All-in-one nanodots formed via carbon dot-mediated and albumin-based synthesis: Multimodal imaging-guided and mild laser-enhanced cancer therapy. *ACS Appl. Mater. Interfaces* **2018**, *10*, 42077–42087.

[12] Zhang, L. S.; Yin, T.; Zhang, B. Z.; Yan, C.; Lu, C. Y.; Liu, L. L.; Chen, Z.; Ran, H.; Shi, Q. X.; Pan, H. et al. Cancer-macrophage hybrid membrane-camouflaged photochlor for enhanced sonodynamic therapy against triple-negative breast cancer. *Nano Res.* **2022**, *15*, 4224–4232.

[13] Hao, Y.; Chen, Y. W.; He, X. L.; Yu, Y. Y.; Han, R. X.; Li, Y.; Yang, C. L.; Hu, D. R.; Qian, Z. Y. Polymeric nanoparticles with ROS-responsive prodrug and platinum nanozyme for enhanced chemophotodynamic therapy of colon cancer. *Adv. Sci.* **2020**, *7*, 2001853.

[14] Allamyradov, Y.; ben Yosef, J.; Annamuradov, B.; Ateyeh, M.; Street, C.; Whipple, H.; Er, A. O. Photodynamic therapy review: Past, present, future, opportunities and challenges. *Photochem* **2024**, *4*, 434–461.

[15] Faes, S.; Santoro, T.; Demartines, N.; Dormond, O. Evolving significance and future relevance of anti-angiogenic activity of mTOR inhibitors in cancer therapy. *Cancers* **2017**, *9*, 152.

[16] Bhaoighill, M. N.; Dunlop, E. A. Mechanistic target of rapamycin inhibitors: Successes and challenges as cancer therapeutics. *Cancer Drug Resist.* **2019**, *2*, 1069–1085.

[17] Mukhopadhyay, S.; Frias, M. A.; Chatterjee, A.; Yellen, P.; Foster, D. A. The enigma of rapamycin dosage. *Mol. Cancer Ther.* **2016**, *15*, 347–353.

[18] Ballou, L. M.; Lin, R. Z. Rapamycin and mTOR kinase inhibitors. *J. Chem. Biol.* **2008**, *1*, 27–36.

[19] Nicolás-Morala, J.; Mascaraque-Checa, M.; Gallego-Rentero, M.; Barahona, A.; Abarca-Lachen, E.; Carrasco, E.; Gilaberte, Y.; González, S.; Juarranz, Á. The m-TORC1 inhibitor Sirolimus increases the effectiveness of Photodynamic therapy in the treatment of cutaneous Squamous Cell Carcinoma, impairing NRF2 antioxidant signaling. *Int. J. Biol. Sci.* **2024**, *20*, 4238–4257.

[20] Lamming, D. W. Inhibition of the mechanistic target of rapamycin (mTOR)-rapamycin and beyond. *Cold Spring Harb. Perspect. Med.* **2016**, *6*, a025924.

[21] Weyergang, A.; Berg, K.; Kaalhus, O.; Peng, Q.; Selbo, P. K. Photodynamic therapy targets the mTOR signaling network *in vitro* and *in vivo*. *Mol. Pharm.* **2009**, *6*, 255–264.

[22] Huang, C.; Lin, B. Q.; Chen, C. Y.; Wang, H. M.; Lin, X. S.; Liu, J. M.; Ren, Q. F.; Tao, J.; Zhao, P.; Xu, Y. K. Synergistic reinforcing of immunogenic cell death and transforming tumor-associated macrophages via a multifunctional cascade bioreactor for optimizing cancer immunotherapy. *Adv. Mater.* **2022**, *34*, 2207593.

[23] Tian, H. P.; Lu, J.; He, H. R.; Zhang, L.; Dong, Y. L.; Yao, H. P.; Feng, W. Y.; Wang, S. W. The effect of Astragalus as an adjuvant treatment in type 2 diabetes mellitus: A (preliminary) meta-analysis. *J. Ethnopharmacol.* **2016**, *191*, 206–215.

[24] Wan, X. H.; Yin, Y. M.; Zhou, C. Z.; Hou, L.; Cui, Q. H.; Zhang, X. P.; Cai, X. Q.; Wang, Y. L.; Wang, L. Z.; Tian, J. Z. Polysaccharides derived from Chinese medicinal herbs: A promising choice of vaccine adjuvants. *Carbohydr. Polym.* **2022**, *276*, 118739.

[25] Zhang, Y.; Li, N.; Gong, H. X.; Zhao, C. J.; Bao, X. R.; Liu, W.; Gao, J.; Zhang, J. L.; Yin, H. S.; Dong, Z. Q. Structural characterization and anti-tumor immunomodulatory effects of polysaccharides from *Astragalus mongholicus* with different cultivation modes. *Int. J. Biol. Macromol.* **2025**, *318*, 145233.

[26] Li, N.; Zhang, Y.; Han, M. M.; Liu, T.; Wu, J. J.; Xiong, Y. X.; Fan, Y. K.; Ye, F.; Jin, B.; Zhang, Y. H. et al. Self-adjuvant *Astragalus* polysaccharide-based nanovaccines for enhanced tumor immunotherapy: A novel delivery system candidate for tumor vaccines. *Sci. China Life Sci.* **2024**, *67*, 680–697.

[27] Shin, W. J.; Noh, H. J.; Noh, Y. W.; Kim, S.; Um, S. H.; Lim, Y. T. Hyaluronic acid-supported combination of water insoluble immunostimulatory compounds for anti-cancer immunotherapy. *Carbohydr. Polym.* **2017**, *155*, 1–10.

[28] Koo, B. I.; Jin, S. M.; Kim, H.; Lee, D. J.; Lee, E.; Nam, Y. S. Conjugation-free multilamellar protein-lipid hybrid vesicles for multifaceted immune responses. *Adv. Healthc. Mater.* **2021**, *10*, 2101239.

[29] Wu, N.; Chen, Q. T.; Zou, Y. J.; Miao, C. Y.; Ma, G. H.; Wu, J. Chitosan particle-emulsion complex adjuvants: The effect of particle distribution on the immune intensity and response type. *Carbohydr. Polym.* **2023**, *309*, 120673.

[30] Liu, X. W.; Guo, C. J.; Yang, W. L.; Wang, W. X.; Diao, N. N.; Cao, M.; Cao, Y. X.; Wang, X. M.; Wang, X. X.; Pei, H. J. et al. Composite microneedles loaded with Astragalus membranaceus polysaccharide nanoparticles promote wound healing by curbing the ROS/NF-κB pathway to regulate macrophage polarization. *Carbohydr. Polym.* **2024**, *345*, 122574.

[31] Tang, Z. J.; Huang, G. L. Extraction, structure, and activity of polysaccharide from Radix astragali. *Biomed. Pharmacother.* **2022**, *150*, 113015.

[32] Cheung, E. C.; Strathdee, D.; Stevenson, D.; Coomes, J.; Blyth, K.; Vousden, K. H. Regulation of ROS signaling by TIGAR induces cancer-modulating responses in the tumor microenvironment. *Proc. Natl. Acad. Sci. USA* **2024**, *121*, e2416076121.

[33] Gao, C.; Huang, Q. X.; Liu, C. H.; Kwong, C. H. T.; Yue, L. D.; Wan, J. B.; Lee, S. M. Y.; Wang, R. B. Treatment of atherosclerosis by macrophage-biomimetic nanoparticles via targeted pharmacotherapy and sequestration of proinflammatory cytokines. *Nat. Commun.* **2020**, *11*, 2622.

[34] Le, T. N.; Mathew, J.; Shen, Y. C.; Ngoc Nguyet, L. N.; Lee, C. K.; Rao, N. V. A polycaprolactone-based nanocarrier containing thioketal

linkers and charge conversion capabilities for doxorubicin delivery. *Polymer* **2025**, *324*, 128223.

[35] Li, S.; Zou, R. F.; Tu, Y. Q.; Wu, J. C.; Landry, M. P. Cholesterol-directed nanoparticle assemblies based on single amino acid peptide mutations activate cellular uptake and decrease tumor volume. *Chem. Sci.* **2017**, *8*, 7552–7559.

[36] Lou, X. F.; Wang, C.; Zhang, J. C.; Du, Y. Z.; Xu, X. L. A melanin-like nanoenzyme for acute lung injury therapy via suppressing oxidative and endoplasmic reticulum stress response. *Pharmaceutics* **2021**, *13*, 1850.

[37] Rui, Y.; Wilson, D. R.; Choi, J.; Varanasi, M.; Sanders, K.; Karlsson, J.; Lim, M.; Green, J. J. Carboxylated branched poly (β-amino ester) nanoparticles enable robust cytosolic protein delivery and CRISPR-Cas9 gene editing. *Sci. Adv.* **2019**, *5*, eaay3255.

[38] Yang, J.; Ren, B. B.; Yin, X. T.; Xiang, L. L.; Hua, Y. Q.; Huang, X.; Wang, H. B.; Mao, Z. W.; Chen, W.; Deng, J. Expanded ROS generation and hypoxia reversal: Excipient-free self-assembled nanotheranostics for enhanced cancer photodynamic immunotherapy. *Adv. Mater.* **2024**, *36*, 2402720.

[39] Lu, S.; Li, Y. F.; Yu, Y. J. Glutathione-scavenging celastrol-Cu nanoparticles induce self-amplified cuproptosis for augmented cancer immunotherapy. *Adv. Mater.* **2024**, *36*, 2404971.

[40] Yang, Z. Z.; Teng, Y. L.; Lin, M.; Peng, Y. W.; Du, Y. T.; Sun, Q.; Gao, D. T.; Yuan, Q.; Zhou, Y.; Yang, Y. L. et al. Reinforced immunogenic endoplasmic reticulum stress and oxidative stress via an orchestrated nanophotoinducer to boost cancer photoimmunotherapy. *ACS Nano* **2024**, *18*, 7267–7286.

[41] Li, J. N.; Wu, T. Z.; Wang, W. D.; Gong, Y. M.; Lu, M. Z.; Zhang, M. M.; Lu, W. Y.; Zhou, Y. M.; Yang, Y. N. Hybrid nanoparticle-mediated simultaneous ROS scavenging and STING activation improve the antitumor immunity of *in situ* vaccines. *Sci. Adv.* **2024**, *10*, eadn3002.

[42] Fu, L.; Su, Z. Y.; Wu, S. Y.; Cheng, Y. F.; Hu, C.; Zhang, J. M. Redox-responsive hyaluronic acid-celastrol prodrug micelles with glycyrrhetinic acid co-delivery for tumor combination therapy. *Chin. Chem. Lett.* **2025**, *36*, 110227.

[43] Hao, Y.; Chen, Y. W.; He, X. L.; Han, R. X.; Yang, C. L.; Liu, T. L.; Yang, Y.; Liu, Q. Y.; Qian, Z. Y. RGD peptide modified platinum nanozyme Co-loaded glutathione-responsive prodrug nanoparticles for enhanced chemo-photodynamic bladder cancer therapy. *Biomaterials* **2023**, *293*, 121975.

[44] Xiang, J. F.; Suo, M.; Lan, J. L.; Ning, S. P.; Liu, H.; Hong, W.; Liang, J.; Zheng, J. Q.; Zhu, D. M.; Mo, J. L. Novel carrier-free nanomedicine for regulating macrophage phenotype to amplify anti-tumor photoimmunotherapy. *Small* **2025**, *21*, e05304.

[45] Li, Y. B.; Jiang, M. Y.; Deng, Z. M.; Zeng, S. J.; Hao, J. H. Low dose soft X-ray remotely triggered lanthanide nanovaccine for deep tissue CO gas release and activation of systemic anti-tumor immunoresponse. *Adv. Sci.* **2021**, *8*, 2004391.

[46] Fan, X. D.; Yue, T. X.; Liu, A. D.; Xie, X. W.; Fang, W. X.; Wei, Y. H.; Zheng, H. S.; Zheng, H. Y.; Zhou, M. Q.; Piao, J. et al. Lignin-assisted construction of sub-10 nm supramolecular self-assembly for photothermal immunotherapy and potentiating anti-PD-1 therapy against primary and distant breast tumors. *Asian J. Pharm Sci.* **2022**, *17*, 713–727.